Mon. Not. R. Astron. Soc. **000**, 1–20 (2014) Printed 9 January 2015 (MN LATEX style file v2.2)

Suppression of extreme orbital evolution in triple systems with short range forces

Bin Liu[1,2⋆], Diego J. Muñoz[2] and Dong Lai[2]
[1] *Center for Astrophysics, University of Science and Technology of China, Hefei, Anhui 230026, People's Republic of China*
[2] *Center for Space Research, Department of Astronomy, Cornell University, Ithaca, NY 14853, USA*

9 January 2015

arXiv:1409.6717v2 [astro-ph.EP] 7 Jan 2015

ABSTRACT
The Lidov-Kozai (LK) mechanism plays an important role in the secular evolution of many hierarchical triple systems. The standard LK mechanism consists of large-amplitude oscillations in eccentricity and inclination of a binary subject to the quadrupole potential from an outer perturber. Recent work has shown that when the octupole terms are included in the potential, the inner binary can reach more extreme eccentricities as well as undergo orientation flips. It is known that pericenter precessions due to short-range effects, such as General Relativity and tidal and rotational distortions, can limit the growth of eccentricity and even suppress standard (quadrupolar) LK oscillations, but their effect on the octupole-level LK mechanism has not been fully explored. In this paper, we systematically study how these short-range forces affect the extreme orbital behaviour found in octupole LK cycles. In general, the influence of the octupole potential is confined to a range of initial mutual inclinations $i_{\rm tot}$ centered around 90° (when the inner binary mass ratio is $\ll 1$), with this range expanding with increasing octupole strength. We find that, while the short-range forces do not change the width and location of this "window of influence", they impose a strict upper limit on the maximum achievable eccentricity. This limiting eccentricity can be calculated analytically, and its value holds even for strong octupole potential and for the general case of three comparable masses. Short-range forces also affect orbital flips, progressively reducing the range of $i_{\rm tot}$ within which flips are possible as the intensity of these forces increases.

Key words: binaries: close – planetary system

1 INTRODUCTION

Three-body systems are ubiquitous in astrophysics, appearing in a wide range of configurations and scales, from planet-satellite systems to black holes in dense stellar clusters. Although the gravitational three-body problem is in general non-integrable, a hierarchical system (i.e., triple configuration consisting of an inner binary orbited by a distant companion) can be simplified by retaining the lowest orders in the multipole expansion of the interaction potentials. In this case, the triple system is represented by two nested binary systems (an "inner binary" and an "outer binary"), with the corresponding orbital elements evolving on secular timescales due to mutual interactions.

Lidov (1962) and Kozai (1962) discovered that when the mutual inclination angle between the inner and outer binaries is sufficiently high, the time-averaged tidal gravitational force from the outer companion can induce large-amplitude oscillations in the eccentricity and inclination of the inner binary[1]. In recent years, numerous works have shown that Lidov–Kozai oscillations could play an important role in the formation and evolution of various astrophysical systems. Examples include: (i) The formation of close stellar binaries, including those containing compact objects (e.g., Mazeh & Shaham 1979; Kiseleva et al. 1998; Eggleton & Kiseleva–Eggleton 2001; Fabrycky & Tremaine 2007; Perets & Fabrycky 2009; Shappee & Thompson 2013; Naoz & Fabrycky 2014); (ii) The excitation of eccentricities of exoplanet systems (e.g., Holman, Touma, & Tremaine 1997; Innanen et al. 1997; Mazeh et al. 1997) and the formation of hot Jupiters through high-eccentricity migration (e.g., Wu & Murray 2003; Fabrycky & Tremaine 2007; Correia et al. 2011; Naoz et al. 2012; Dong, Katz, & Socrates 2014; Storch et al. 2014; Petrovich 2014); (iii) The production of Type Ia

⋆ E-mail: bl559@cornell.edu

[1] Lidov considered the long-term evolution of satellite orbits under the perturbation of the Moon, while Kozai studied the evolution of asteroid orbits under the perturbation of Jupiter.

© 2014 RAS

supernovae from white-dwarf binary mergers (e.g., Thompson 2011; Prodan, Murray, & Thompson 2013) or direct collisions (e.g., Katz & Dong 2012; Kushnir et al. 2013); (iv) The properties of irregular satellites (particularly their inclination distribution relative to the ecliptic) of giant planets in the solar system (e.g., Carruba et al. 2002; Nesvorný et al. 2003); (v) The formation and merger of (stellar and supermassive) black hole binaries at the centers globular clusters or galaxies (e.g., Blaes et al. 2002; Miller & Hamilton 2002; Wen 2003; Antonini, Murray & Mikkola 2014).

The simplest Lidov–Kozai mechanism involves a test mass ("planet") orbiting a primary body ("star") perturbed by an external companion, with the interaction potential truncated to the quadrupole order. In this test-mass, quadrupole approximation, the projected angular momentum (along the external binary axis) of the planet is conserved. If the influence of other short-range forces (SRFs) is negligible, the maximum eccentricity achieved by the inner binary (for an initially very small eccentricity) during the Lidov–Kozai oscillation is given by

$$e_{\max} = \left(1 - \frac{5}{3}\cos^2 i_0\right)^{1/2} \tag{1}$$

where i_0 is the initial inclination angle of the two orbits. Thus Lidov–Kozai oscillation requires i_0 to lie between $\cos^{-1}\sqrt{3/5} \simeq 39^\circ$ and 141°. It has been recognized that the Lidov–Kozai cycles can be suppressed by other short-range effects that induce periapse precession of the inner binary, including the precessions due to General Relativity (GR), rotational bulge and tidal distortion (e.g., Holman, Touma, & Tremaine 1997; Dong, Katz, & Socrates 2014). The suppression arises because these additional precessions tend to destroy the near 1 : 1 resonance between the longitude of the periapse ω and the longitude of the ascending node Ω required for eccentricity excitation. Thus, the maximum eccentricity can be reduced from the "pure" Lidov–Kozai value (Equation 1).

It has also been recognized that high-order expansion of the interaction potential can lead to a much richer dynamical behaviour of hierarchical triples than the simplest Lidov–Kozai oscillation based on the test-mass, quadrupole approximation. Harrington (1968); Marchal et al. (1990); Krymolowski & Mazeh (1999); Ford et al. (2000b); Blaes et al. (2002) have derived the orbit-averaged Hamiltonian to octupole order and used the resulting equation of motion to explore some aspects of the evolution of triples. Unlike the pure quadrupole case, the projected angular momentum of the inner binary (even in the test-mass limit) is no longer constant when the octupole potential is included (the octupole potential is nonzero when the outer binary is eccentric and the components of the inner binary have different masses). Therefore, the secular dynamics of triples is generally not integrable in the octupole order and may lead to chaos (e.g., Li et al. 2014b). Recent works have examined the rich dynamical behaviour of such "eccentric" Lidov–Kozai mechanism, either numerically (e.g., Naoz et al. 2011, 2013b; Teyssandier et al. 2013; Li et al. 2014a) or semi-analytically (e.g., Katz, Dong, & Malhotra 2011; Lithwick & Naoz 2011), and explored their implications for the formation of hot Jupiters and the resulting spin-orbit misalignments (e.g., Naoz et al. 2011, 2012; Petrovich 2014).

The works cited above have revealed two important consequences of the "eccentric" Lidov–Kozai mechanism: (i) The eccentricity of the inner binary can be driven to extreme value ($1 - e \sim 10^{-6}$) even for "modest" initial orbital inclinations; (ii) The inner orbit can flip and come retrograde relative to the outer orbit. These two effects are related, as orbital flip is often associated with extreme eccentricity. Since the precession of periapse due to short-range forces is strongly dependent on eccentricity, it is not clear to what extent the extreme eccentricity can be realized in realistic situations. While short-range effects were included in some population synthesis calculations for the formation of hot Jupiters (e.g., Naoz et al. 2012; Petrovich 2014), a systematic study of the short-range force effects on eccentric Lidov–Kozai mechanism is currently lacking.

In this paper, by running a sequence of numerical integrations, we study how SRFs affect the evolution of the inner binary (with and without the test-mass approximation), including the interaction potential up to the octupole order. Combining with various analytical considerations, we characterize the parameters space systematically to understand how the maximum eccentricity is modified by the SRFs.

Our paper is organized as follows. In Section 2, we derive the secular equations of motion up to the octupole order using a vectorial formalism. In Section 3, we provide a brief overview of short-range effects, estimating the maximum eccentricity allowed by the presence of various SRFs. In Section 4, we describe our numerical integrations, carried out over a range of parameters for triple systems consisting of a star-planet binary and an outer stellar companion. In Section 5, we extend our analysis to triple systems in which all components have comparable masses. We summarize our main results in Section 6.

2 EVOLUTION OF TRIPLE SYSTEMS IN THE SECULAR APPROXIMATION

In a hierarchical triple system, two bodies of masses m_0 and m_1 orbit each other (with semimajor axis a_1) while a third body of mass m_2 orbits the center mass of the inner bodies (m_0 and m_1) on a wider orbit (with semimajor axis a_2). The complete Hamiltonian of the system can then be written as the sum of the individual Hamiltonians of the inner and outer orbits plus an interaction potential Φ (e.g., Harrington 1968):

$$\begin{aligned}\mathcal{H} = &\ \mathcal{H}_1 + \mathcal{H}_2 + \Phi \\ = &-\frac{Gm_0m_1}{2a_1} - \frac{Gm_2(m_0+m_1)}{2a_2} \\ &-\frac{G}{a_2}\sum_{l=2}^{\infty}\left(\frac{a_1}{a_2}\right)^l M_l \left(\frac{|\mathbf{r}_1|}{a_1}\right)^l \left(\frac{a_2}{|\mathbf{r}_2|}\right)^{l+1} P_l(\cos\theta)\ .\end{aligned} \tag{2}$$

where $\mathbf{r_1}$ is the instantaneous separation vector between the inner masses m_0 and m_1, $\mathbf{r_2}$ is the instantaneous separation vector between m_2 and center of mass of m_0 and m_1, and θ is the angle between $\mathbf{r}_1$ and $\mathbf{r}_2$. In Equation (2), $P_l(x)$ is the Legendre polynomial of degree l and M_l is a coefficient that depends on m_0, m_1, m_2 and l.

If m_2 is sufficiently distant (i.e., $a_2 \gg a_1$), only the smallest values of l contribute significantly to Φ, and the coupling term is weak such that the inner and outer Keplerian orbits change very slowly (on timescales much longer

than their orbital periods). In this regime, the secular approximation is valid, meaning that, the system can be adequately described by two slowly evolving Keplerian orbits, while the short timescale behaviour of the three individual trajectories is irrelevant (e.g., Marchal et al. 1990).

This perturbative method has been used extensively to study three-body systems up to quadrupole ($l = 2$)(e.g., Kozai 1962; Lidov 1962) and octupole ($l = 3$) orders (e.g., Ford et al. 2000b; Lithwick & Naoz 2011; Naoz et al. 2013b). Most of these studies have used the classical perturbation methods of celestial mechanics, based on an orbital-element formulation of the Hamiltonian system. In the following, we present the secular evolution equations to the octupole order using a geometric (vectorial) formalism (e.g. Tremaine et al. 2009; Correia et al. 2011; Tremaine & Yavetz 2014), and confirm via angular projections that they are equivalent to Hamilton's equations for the orbital elements.

2.1 Equations of motion in vector form

In vector form, the instantaneous position $\mathbf{r}$ of a body in Keplerian motion can be written as

$$\mathbf{r} = r(\cos f\,\hat{\mathbf{u}} + \sin f\,\hat{\mathbf{v}}) \tag{3}$$

with $r = a(1-e^2)/(1+e\cos f)$, where a, e and f are the semimajor axis, eccentricity and true anomaly, respectively. The orthogonal unit vectors $\hat{\mathbf{u}}$ and $\hat{\mathbf{v}}$ define the orbital plane, where $\hat{\mathbf{u}}$ points in the direction of pericenter (i.e., at $f = 0$). A third unit vector $\hat{\mathbf{n}}$, pointed in the direction of the orbital angular momentum, completes an orthonormal triad, $\hat{\mathbf{u}} \times \hat{\mathbf{v}} = \hat{\mathbf{n}}$. Alternatively, it is often useful to work in terms of the dimensionless angular momentum vector $\mathbf{j}$ and the eccentricity vector $\mathbf{e}$:

$$\mathbf{j} = \sqrt{1-e^2}\hat{\mathbf{n}}\ , \qquad \mathbf{e} = e\hat{\mathbf{u}}\ . \tag{4}$$

where $\mathbf{j}$ and $\mathbf{e}$ satisfy $\mathbf{j}\cdot\mathbf{e} = 0$ and $\mathbf{j}^2 + \mathbf{e}^2 = 1$.

Truncating the interaction potential (Equation 2) at the $l = 3$ order, we write $\Phi = \Phi_{\rm Quad} + \Phi_{\rm Oct}$, where the quadrupole term is

$$\Phi_{\rm Quad} = -\frac{Gm_0m_1m_2}{(m_0+m_1)r_2}\left[\frac{3}{2}\frac{(\mathbf{r}_1\cdot\mathbf{r}_2)^2}{r_2^4} - \frac{r_1^2}{2r_2^2}\right], \tag{5}$$

and the octupole term is

$$\Phi_{\rm Oct} = -\frac{Gm_0m_1m_2(m_0-m_1)}{(m_0+m_1)^2r_2}\left[\frac{5}{2}\frac{(\mathbf{r}_1\cdot\mathbf{r}_2)^3}{r_2^6} - \frac{3}{2}\frac{r_1^2(\mathbf{r}_1\cdot\mathbf{r}_2)}{r_2^4}\right], \tag{6}$$

and where the position vectors $\mathbf{r}_1$ and $\mathbf{r}_2$ track two different Keplerian orbits (Equation 3) of orbital elements a_1 and e_1 (inner) and a_2 and e_2 (outer), which are oriented in space by the triads $(\hat{\mathbf{u}}_1, \hat{\mathbf{v}}_1, \hat{\mathbf{n}}_1)$ and $(\hat{\mathbf{u}}_2, \hat{\mathbf{v}}_2, \hat{\mathbf{n}}_2)$, respectively.

The next step is to filter out the high-frequency behaviour by time-averaging the quadrupole and octupole potentials twice: over the inner orbital period and the outer orbital period. Using a standard averaging procedure (e.g. Tremaine & Yavetz 2014), we find that the double averaged quadrupole potential is given by

$$\langle\Phi_{\rm Quad}\rangle = \frac{\mu_1\Phi_0}{8}\left[1-6e_1^2-3(1-e_1^2)(\hat{\mathbf{n}}_1\cdot\hat{\mathbf{n}}_2)^2+15e_1^2(\hat{\mathbf{u}}_1\cdot\hat{\mathbf{n}}_2)^2\right], \tag{7}$$

where $\mu_1 = m_0m_1/(m_0+m_1)$ is the reduced mass of the inner orbit. The double-averaged octupole potential is

$$\begin{aligned}\langle\Phi_{\rm Oct}\rangle =& \frac{15\mu_1\Phi_0\varepsilon_{\rm Oct}}{64}\Bigg\{e_1(\hat{\mathbf{u}}_1\cdot\hat{\mathbf{u}}_2)\Big[8e_1^2 - 1 - 35e_1^2(\hat{\mathbf{u}}_1\cdot\hat{\mathbf{n}}_2)^2 \\ &+ 5(1-e_1^2)(\hat{\mathbf{n}}_1\cdot\hat{\mathbf{n}}_2)^2\Big] \\ &+ 10e_1(1-e_1^2)(\hat{\mathbf{u}}_1\cdot\hat{\mathbf{n}}_2)(\hat{\mathbf{n}}_1\cdot\hat{\mathbf{u}}_2)(\hat{\mathbf{n}}_1\cdot\hat{\mathbf{n}}_2)\Bigg\}\ .\end{aligned} \tag{8}$$

In Equations (7) and (8) we have defined the coefficients

$$\Phi_0 \equiv \frac{Gm_2a_1^2}{a_2^3(1-e_2^2)^{3/2}} \tag{9}$$

and

$$\varepsilon_{\rm Oct} \equiv \frac{m_0-m_1}{m_0+m_1}\frac{a_1}{a_2}\frac{e_2}{1-e_2^2}\ , \tag{10}$$

where the magnitude of $\varepsilon_{\rm Oct}$ quantifies the importance of the octupole term relative to the quadrupole term.

In terms of the averaged potentials, the equations of motion for the orbital vectors $\mathbf{j}_1$, $\mathbf{e}_1$, $\mathbf{j}_2$ and $\mathbf{e}_2$ (defined as in Equation 4 for the inner and outer orbits) are

$$\frac{d\mathbf{j}_1}{dt} = -\frac{1}{L_1}\left(\mathbf{j}_1\times\nabla_{\mathbf{j}_1}\langle\Phi\rangle + \mathbf{e}_1\times\nabla_{\mathbf{e}_1}\langle\Phi\rangle\right), \tag{11}$$

$$\frac{d\mathbf{e}_1}{dt} = -\frac{1}{L_1}\left(\mathbf{j}_1\times\nabla_{\mathbf{e}_1}\langle\Phi\rangle + \mathbf{e}_1\times\nabla_{\mathbf{j}_1}\langle\Phi\rangle\right), \tag{12}$$

$$\frac{d\mathbf{j}_2}{dt} = -\frac{1}{L_2}\left(\mathbf{j}_2\times\nabla_{\mathbf{j}_2}\langle\Phi\rangle + \mathbf{e}_2\times\nabla_{\mathbf{e}_2}\langle\Phi\rangle\right), \tag{13}$$

$$\frac{d\mathbf{e}_2}{dt} = -\frac{1}{L_2}\left(\mathbf{j}_2\times\nabla_{\mathbf{e}_2}\langle\Phi\rangle + \mathbf{e}_2\times\nabla_{\mathbf{j}_2}\langle\Phi\rangle\right). \tag{14}$$

Here, L_1 and L_2 are

$$L_1 = \mu_1\sqrt{G(m_0+m_1)a_1}, \tag{15}$$

$$L_2 = \mu_2\sqrt{G(m_0+m_1+m_2)a_2}\ , \tag{16}$$

where μ_2 is the reduced mass of the outer orbit $\mu_2 = (m_0+m_1)m_2/(m_0+m_1+m_2)$.

Substituting Equations (7) and (8) into (11)–(14), the octupole-level secular evolution equations can be obtained.

For the inner orbit, we have

$$\begin{aligned}\frac{d\mathbf{j}_1}{dt} =& \frac{3}{4\,t_K}\Big[(\mathbf{j}_1\cdot\hat{\mathbf{n}}_2)\,\mathbf{j}_1\times\hat{\mathbf{n}}_2 - 5(\mathbf{e}_1\cdot\hat{\mathbf{n}}_2)\,\mathbf{e}_1\times\hat{\mathbf{n}}_2\Big] \\ &- \frac{75\varepsilon_{\rm Oct}}{64\,t_K}\Bigg\{\Big[2\Big[(\mathbf{e}_1\cdot\hat{\mathbf{u}}_2)(\mathbf{j}_1\cdot\hat{\mathbf{n}}_2) \\ &+ (\mathbf{e}_1\cdot\hat{\mathbf{n}}_2)(\mathbf{j}_1\cdot\hat{\mathbf{u}}_2)\Big]\,\mathbf{j}_1 + 2\Big[(\mathbf{j}_1\cdot\hat{\mathbf{u}}_2)(\mathbf{j}_1\cdot\hat{\mathbf{n}}_2) \\ &- 7(\mathbf{e}_1\cdot\hat{\mathbf{u}}_2)(\mathbf{e}_1\cdot\hat{\mathbf{n}}_2)\Big]\,\mathbf{e}_1\Big]\times\hat{\mathbf{n}}_2 \\ &+ \Big[2(\mathbf{e}_1\cdot\hat{\mathbf{n}}_2)(\mathbf{j}_1\cdot\hat{\mathbf{n}}_2)\,\mathbf{j}_1 + \Big[\frac{8}{5}e_1^2 - \frac{1}{5} \\ &- 7(\mathbf{e}_1\cdot\hat{\mathbf{n}}_2)^2 + (\mathbf{j}_1\cdot\hat{\mathbf{n}}_2)^2\Big]\,\mathbf{e}_1\Big]\times\hat{\mathbf{u}}_2\Bigg\},\end{aligned} \tag{17}$$

$$\frac{d\mathbf{e}_1}{dt} = \frac{3}{4\,t_K}\Big[(\mathbf{j}_1\cdot\hat{\mathbf{n}}_2)\;\mathbf{e}_1\times\hat{\mathbf{n}}_2 + 2\,\mathbf{j}_1\times\mathbf{e}_1 - 5(\mathbf{e}_1\cdot\hat{\mathbf{n}}_2)\mathbf{j}_1\times\hat{\mathbf{n}}_2\Big] - \frac{75\varepsilon_{\rm Oct}}{64\,t_K}\Bigg\{\Big[2(\mathbf{e}_1\cdot\hat{\mathbf{n}}_2)(\mathbf{j}_1\cdot\hat{\mathbf{n}}_2)\;\mathbf{e}_1 + \Big[\frac{8}{5}e_1^2 - \frac{1}{5} - 7(\mathbf{e}_1\cdot\hat{\mathbf{n}}_2)^2 + (\mathbf{j}_1\cdot\hat{\mathbf{n}}_2)^2\Big]\;\mathbf{j}_1\Big]\times\hat{\mathbf{u}}_2 + \Big[2\Big[(\mathbf{e}_1\cdot\hat{\mathbf{u}}_2)(\mathbf{j}_1\cdot\hat{\mathbf{n}}_2) + (\mathbf{e}_1\cdot\hat{\mathbf{n}}_2)(\mathbf{j}_1\cdot\hat{\mathbf{u}}_2)\Big]\;\mathbf{e}_1 + 2\Big[(\mathbf{j}_1\cdot\hat{\mathbf{n}}_2)(\mathbf{j}_1\cdot\hat{\mathbf{u}}_2) - 7(\mathbf{e}_1\cdot\hat{\mathbf{n}}_2)(\mathbf{e}_1\cdot\hat{\mathbf{u}}_2)\Big]\;\mathbf{j}_1\Big]\times\hat{\mathbf{n}}_2 + \frac{16}{5}(\mathbf{e}_1\cdot\hat{\mathbf{u}}_2)\;\mathbf{j}_1\times\mathbf{e}_1\Bigg\}\;. \tag{18}$$

For the outer orbit, we have

$$\frac{d\mathbf{j}_2}{dt} = \frac{3}{4t_K}\frac{L_1}{L_2}\Big[(\mathbf{j}_1\cdot\hat{\mathbf{n}}_2)\;\hat{\mathbf{n}}_2\times\mathbf{j}_1 - 5(\mathbf{e}_1\cdot\hat{\mathbf{n}}_2)\;\hat{\mathbf{n}}_2\times\mathbf{e}_1\Big] - \frac{75\varepsilon_{\rm Oct}}{64t_K}\frac{L_1}{L_2}\Bigg\{2\Big[(\mathbf{e}_1\cdot\hat{\mathbf{n}}_2)(\mathbf{j}_1\cdot\hat{\mathbf{u}}_2)\;\hat{\mathbf{n}}_2 + (\mathbf{e}_1\cdot\hat{\mathbf{u}}_2)(\mathbf{j}_1\cdot\hat{\mathbf{n}}_2)\;\hat{\mathbf{n}}_2 + (\mathbf{e}_1\cdot\hat{\mathbf{n}}_2)(\mathbf{j}_1\cdot\hat{\mathbf{n}}_2)\;\hat{\mathbf{u}}_2\Big]\times\mathbf{j}_1 + \Big[2(\mathbf{j}_1\cdot\hat{\mathbf{u}}_2)(\mathbf{j}_1\cdot\hat{\mathbf{n}}_2)\;\hat{\mathbf{n}}_2 - 14(\mathbf{e}_1\cdot\hat{\mathbf{u}}_2)(\mathbf{e}_1\cdot\hat{\mathbf{n}}_2)\;\hat{\mathbf{n}}_2 + \Big[\frac{8}{5}e_1^2 - \frac{1}{5} - 7(\mathbf{e}_1\cdot\hat{\mathbf{n}}_2)^2 + (\mathbf{j}_1\cdot\hat{\mathbf{n}}_2)^2\Big]\;\hat{\mathbf{u}}_2\Big]\times\mathbf{e}_1\Bigg\}, \tag{19}$$

$$\frac{d\mathbf{e}_2}{dt} = \frac{3}{4t_K\sqrt{1-e_2^2}}\frac{L_1}{L_2}\Big[(\mathbf{j}_1\cdot\hat{\mathbf{n}}_2)\;\mathbf{e}_2\times\mathbf{j}_1 - 5(\mathbf{e}_1\cdot\hat{\mathbf{n}}_2)\mathbf{e}_2\times\mathbf{e}_1 - \Big[\frac{1}{2} - 3e_1^2 + \frac{25}{2}(\mathbf{e}_1\cdot\hat{\mathbf{n}}_2)^2 - \frac{5}{2}(\mathbf{j}_1\cdot\hat{\mathbf{n}}_2)^2\Big]\hat{\mathbf{n}}_2\times\mathbf{e}_2\Big] - \frac{75}{64t_K}\frac{\varepsilon_{\rm Oct}}{\sqrt{1-e_2^2}}\frac{L_1}{L_2}\Bigg\{2\Big[(\mathbf{e}_1\cdot\hat{\mathbf{n}}_2)(\mathbf{j}_1\cdot\mathbf{e}_2)\;\hat{\mathbf{u}}_2 + (\mathbf{j}_1\cdot\hat{\mathbf{n}}_2)(\mathbf{e}_1\cdot\mathbf{e}_2)\;\hat{\mathbf{u}}_2 + \frac{1-e_2^2}{e_2}(\mathbf{e}_1\cdot\hat{\mathbf{n}}_2)(\mathbf{j}_1\cdot\hat{\mathbf{n}}_2)\;\hat{\mathbf{n}}_2\Big]\times\mathbf{j}_1 + \Big[2(\mathbf{j}_1\cdot\mathbf{e}_2)(\mathbf{j}_1\cdot\hat{\mathbf{n}}_2)\;\hat{\mathbf{u}}_2 - 14(\mathbf{e}_1\cdot\mathbf{e}_2)(\mathbf{e}_1\cdot\hat{\mathbf{n}}_2)\;\hat{\mathbf{u}}_2 + \frac{1-e_2^2}{e_2}\Big[\frac{8}{5}e_1^2 - \frac{1}{5} - 7(\mathbf{e}_1\cdot\hat{\mathbf{n}}_2)^2 + (\mathbf{j}_1\cdot\hat{\mathbf{n}}_2)^2\Big]\;\hat{\mathbf{n}}_2\Big]\times\mathbf{e}_1 - \Big[2\Big(\frac{1}{5} - \frac{8}{5}e_1^2\Big)(\mathbf{e}_1\cdot\hat{\mathbf{u}}_2)\;\mathbf{e}_2 + 14(\mathbf{e}_1\cdot\hat{\mathbf{n}}_2)(\mathbf{j}_1\cdot\hat{\mathbf{u}}_2)(\mathbf{j}_1\cdot\hat{\mathbf{n}}_2)\;\mathbf{e}_2 + 7(\mathbf{e}_1\cdot\hat{\mathbf{u}}_2)\Big[\frac{8}{5}e_1^2 - \frac{1}{5} - 7(\mathbf{e}_1\cdot\hat{\mathbf{n}}_2)^2 + (\mathbf{j}_1\cdot\hat{\mathbf{n}}_2)^2\Big]\;\mathbf{e}_2\Big]\times\hat{\mathbf{n}}_2\Bigg\}\;. \tag{20}$$

In the above, we have defined the (quadrupole) Kozai timescale as

$$t_K \equiv \frac{L_1}{\mu_1\Phi_0} = \frac{1}{n_1}\left(\frac{m_0+m_1}{m_2}\right)\left(\frac{a_2}{a_1}\right)^3(1-e_2^2)^{3/2}\;, \tag{21}$$

where $n_1 \equiv \sqrt{G(m_0+m_1)/a_1^3}$ is the mean motion of the inner binary. Equations (17)–(20) describe the long-term evolution of the inner and outer binaries for all mass ratios. Our equations are equivalent to those presented in Petrovich (2014), although they are in a somewhat different form.

Often times, the triple system contains a body of much smaller mass than the other two, such as in the case of a planet around one member of a binary. In this case, the planet can be considered to be a particle of effective zero mass to a very good approximation. In this "test-particle limit" (e.g. Lithwick & Naoz 2011; Katz, Dong, & Malhotra 2011; Naoz et al. 2013b), the outer orbit contains the totality of the angular momentum in the system, and consequently remains fixed in time. To derive the test-particle limit from Equations (17)–(20), we take the limit $L_1/L_2 \to 0$, for which we confirm that $d\mathbf{j}_2/dt = d\mathbf{e}_2/dt = 0$. In this case, the triad $(\hat{\mathbf{x}},\hat{\mathbf{y}},\hat{\mathbf{z}})$ is fixed in space, thus, for the sake of clarity, we relabel these vectors with lab-frame coordinates $(\hat{\mathbf{x}},\hat{\mathbf{y}},\hat{\mathbf{z}})$ in Equations (17)–(18) and in Equations (7) and (8). With these replacements, we recover the expressions of Katz, Dong, & Malhotra (2011) for the potentials and for $d\mathbf{j}_1/dt$ and $\mathbf{e}_1/dt$ for a test particle.

2.2 Equations of motion in orbital elements form

The secular equations for the orbital elements of the inner and outer orbits have been the focus of previous work on hierarchical triple systems (Ford et al. 2000b; Naoz et al. 2011). With the introduction of Delaunay variables, conjugate pairs of coordinates and momenta can be defined, the equations of motion of the orbital elements can be directly derived using Hamilton's equations (e.g. Murray & Dermott 1999).

Instead of using Hamilton equations, one can convert the vector equations (Equations 17–20) into the orbital element form by expressing the Cartesian components of the vectors $\mathbf{j}_\alpha$, $\mathbf{e}_\alpha$ (with $\alpha = 1,2$) in terms of the orbital eccentricity e_α, inclination i_α, argument of periapse ω_α and longitude of ascending nodes Ω_α (e.g. Murray & Dermott 1999):

$$\mathbf{j}_\alpha = \sqrt{1-e_\alpha^2}\begin{pmatrix}\sin i_\alpha\sin\Omega_\alpha\\ -\sin i_\alpha\cos\Omega_\alpha\\ \cos i_\alpha\end{pmatrix}, \tag{22}$$

$$\mathbf{e}_\alpha = e_\alpha\begin{pmatrix}\cos\omega_\alpha\cos\Omega_\alpha - \sin\omega_\alpha\cos i_\alpha\sin\Omega_\alpha\\ \cos\omega_\alpha\sin\Omega_\alpha + \sin\omega_\alpha\cos i_\alpha\cos\Omega_\alpha\\ \sin\omega_\alpha\sin i_\alpha\;.\end{pmatrix}, \tag{23}$$

Here the angles are defined respect to a fixed coordinate frame in which z-axis is aligned with the (conserved) total angular momentum, while the x-y plane coincides with the so-called invariable plane. Thus the relative inclination between the two orbits is $i_{\rm tot} \equiv i_1 + i_2$. Because of angular momentum conservation, the condition $\Delta\Omega = \Omega_1 - \Omega_2 = \pi$ is satisfied.

By substituting Equations (22) and (23) into Equations (17)–(20), we can solve for de_α/dt, di_α/dt, $d\omega_\alpha/dt$ and $d\Omega_\alpha/dt$ (for $\alpha = 1,2$). Since $d\Omega_1/dt = d\Omega_2/dt$, the system is determined by seven independent differential equations. These equations are listed in Appendix A (see Equations A1–A9). Although different in form, we have checked that these

equations are equivalent to those presented by Naoz et al. (2013b).

For the test mass case ($m_1 \ll m_0$), we take the limit $L_1/L_2 \to 0$ in Equations (A1)–(A9). Also, note that in this limit, $\varepsilon_{\rm Oct} \to (a_1/a_2)e_2/(1-e_2^2)$, $i_1 \to i_{\rm tot}$, $i_2 \to 0$. We choose $\hat{\mathbf{u}}_2 = \hat{\mathbf{x}}$, $\hat{\mathbf{v}}_2 = \hat{\mathbf{y}}$, $\hat{\mathbf{n}}_2 = \hat{\mathbf{z}}$ and $\varpi_2 = 0$, where $\omega_2 = \varpi_2 - \Omega_2 = \varpi_2 - \Omega_1 + \pi$. Accordingly, the secular evolution equations become

$$\begin{aligned}\frac{de_1}{d\tau} &= \frac{15}{8} e_1 \sqrt{1-e_1^2}\sin^2 i_1 \sin 2\omega_1 \\ &- \frac{15\sqrt{1-e_1^2}\varepsilon_{\rm Oct}}{512}\Big\{ \cos\Omega_1 \Big[(4+3e_1^2)(3+5\cos 2i_1) \\ &\times \sin\omega_1 + 210\ e_1^2 \sin^2 i_1 \sin 3\omega_1\Big] + 2\cos i_1 \\ &\times \cos\omega_1 \sin\Omega_1 \Big[15(2+5e_1^2)\cos 2i_1 \\ &+ 7(30e_1^2 \cos 2\omega_1 \sin^2 i_1 - 2 - 9e_1^2)\Big]\Big\},\end{aligned} \tag{24}$$

$$\begin{aligned}\frac{di_1}{d\tau} &= -\frac{15}{16}\frac{e_1^2 \sin 2i_1 \sin 2\omega_1}{\sqrt{1-e_1^2}} + \frac{15\ e_1\varepsilon_{\rm Oct}}{256\sqrt{1-e_1^2}} \\ &\times \Big\{ 10\sin 2i_1 \cos\Omega_1 \sin\omega_1 (2+5e_1^2+7e_1^2\cos 2\omega_1) \\ &- \cos\omega_1 \sin i_1 \sin\Omega_1 \Big[26 + 37e_1^2 - 35e_1^2\cos 2\omega_1 \\ &- 15\cos 2i_1 (7e_1^2 \cos 2\omega_1 - 2 - 5e_1^2)\Big]\Big\},\end{aligned} \tag{25}$$

$$\begin{aligned}\frac{d\Omega_1}{d\tau} &= \frac{3}{4}\frac{\cos i_1 (5e_1^2\cos^2\omega_1 - 4e_1^2 - 1)}{\sqrt{1-e_1^2}} \\ &+ \frac{15\ e_1\varepsilon_{\rm Oct}}{128\sqrt{1-e_1^2}}\Big\{ 20\cos i_1 \cos\omega_1 (2+5e_1^2-7e_1^2\cos 2\omega_1) \\ &\times \cos\Omega_1 + \Big[35e_1^2(1+3\cos 2i_1)\cos 2\omega_1 - 46 \\ &- 17e_1^2 - 15(6+e_1^2)\cos 2i_1\Big]\sin\omega_1 \sin\Omega_1\Big\},\end{aligned} \tag{26}$$

$$\begin{aligned}\frac{d\omega_1}{d\tau} &= \frac{3}{4}\frac{2(1-e_1^2)+5\sin^2\omega_1(e_1^2-\sin^2 i_1)}{\sqrt{1-e_1^2}} \\ &+ \frac{15\varepsilon_{\rm Oct}}{64}\Big\{ \frac{e_1\cos i_1}{\sqrt{1-e_1^2}}\Big[\sin\omega_1 \sin\Omega_1 \\ &\times \Big[10(3\cos^2 i_1 - 1)(1-e_1^2) + A\Big] - 5B\cos i_1 \cos\Theta\Big] \\ &- \frac{\sqrt{1-e_1^2}}{e_1}\Big[10\sin\omega_1 \sin\Omega_1 \cos i_1 \\ &\times \sin^2 i_1 (1-3e_1^2) + \cos\Theta(3A - 10\cos^2 i_1 + 2)\Big]\Big\},\end{aligned} \tag{27}$$

where we have introduced the dimensionless time $\tau \equiv t/t_K$ and

$$A \equiv 4 + 3e_1^2 - \frac{5}{2}B\sin^2 i_1\ , \tag{28}$$

$$B \equiv 2 + 5e_1^2 - 7e_1^2\cos 2\omega_1\ , \tag{29}$$

$$\cos\Theta \equiv \cos\omega_1 \cos\Omega_1 - \cos i_1 \sin\omega_1 \sin\Omega_1\ . \tag{30}$$

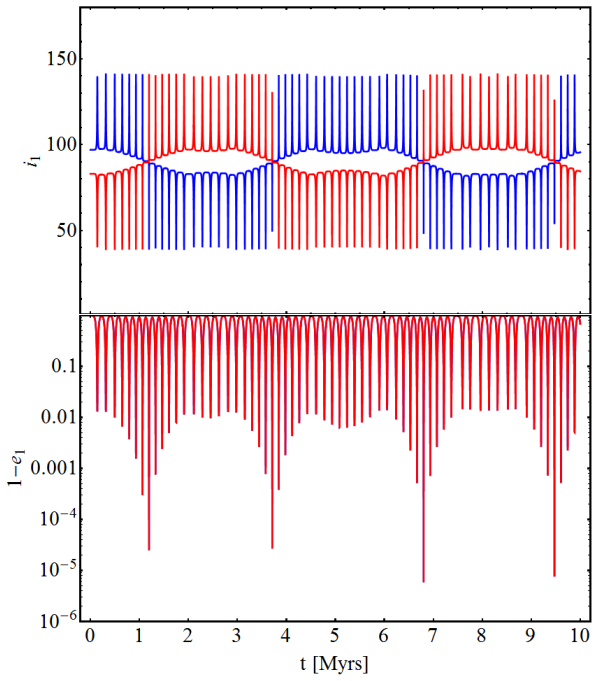

Figure 1. Evolution of inclination i_1 and eccentricity e_1 from numerical integration of Equations (24)–(27) for a prograde (red) and a retrograde (blue) inner binary. The system parameters are $m_0 = 1M_\odot$, $m_1 \ll m_0$, $m_2 = 1M_\odot$, $a_1 = 1$AU, $a_2 = 100$AU and $e_2 = 0.8$. We set $e_1 = 10^{-3}$ initially. Inclinations are initialized at $\pm 7°$ from 90°. Red lines: $i_{\rm tot} = i_1 = 83°$, $\omega = 0°$, $\Omega = 180°$; Blue lines: $i_{\rm tot} = i_1 = 97°$, $\omega = 180°$, $\Omega = 0°$. In the lower panel, the blue and red curves exactly overlap.

When the octupole terms are ignored (i.e., $\varepsilon_{\rm Oct} = 0$), Equations (24)–(27) reduce to the orbital element equations of motion found in Innanen et al. (1997, Eqs. 5) for Lidov-Kozai oscillations[2].

2.3 Reflection symmetry of the equations of motion

In the test-particle limit ($m_1 \ll m_0$), the vector equations (17)–(18) are symmetric under reflections of the inner binary. If we perform the replacement $\mathbf{j}_1 \to -\mathbf{j}_1$ (leaving $\mathbf{e}_1$ unchanged), we find that $d\mathbf{j}_1/dt \to -d\mathbf{j}_1/dt$ and $d\mathbf{e}_1/dt \to -d\mathbf{e}_1/dt$, which may be interpreted as reversing the direction of time. In terms of orbital elements, this reflection operation is equivalent to changing $i_1 \to \pi - i_1$, $\omega_1 \to \pi - \omega_1$ and $\Omega_1 \to \Omega_1 + \pi$. Performing this replacement in Equations (24)–(27), we obtain $de_1/d\tau \to -de_1/d\tau$, $di_1/d\tau \to -di_1/d\tau$, $d\Omega_1/d\tau \to -d\Omega_1/d\tau$ and $d\omega_1/d\tau \to -d\omega_1/d\tau$, as expected.

Figure 1 shows the integration of Equations (24)–(27) for two configurations differing solely on the orientation of the $\mathbf{j}_1$ vector (this reflection is carried out by changing the initial conditions $i_{1,0} \to \pi - i_{1,0}$, $\omega_{1,0} \to \pi - \omega_{1,0}$ and

[2] Note that, due to a formatting error, the evolution equation for ω_1 in Innanen et al. (1997) appears with the term $\sqrt{1-e_1^2}$ in the numerator instead of the denominator.

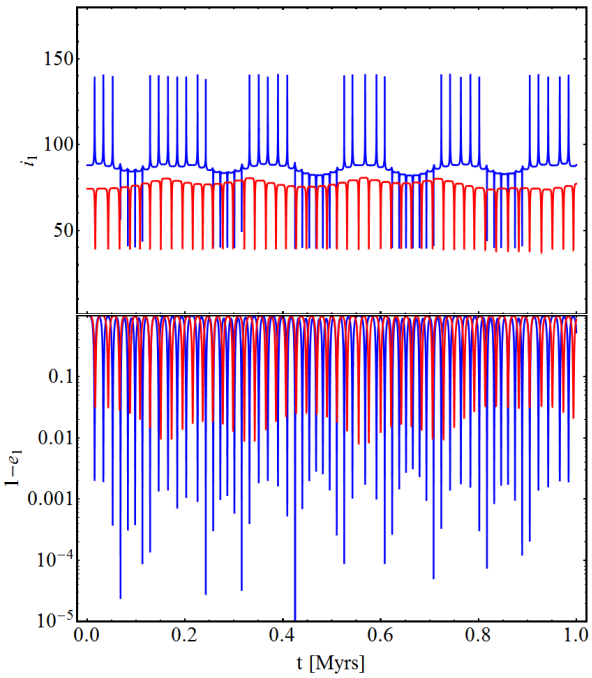

Figure 2. As in Figure 1, evolution of inclination i_1 and eccentricity e_1 from numerical integration of Equations (A1)–(A9) for prograde (red) and retrograde (blue) inner binaries, this time for a general triple with comparable masses. The system parameters are $m_0 = 1M_\odot$, $m_1 = 0.5M_\odot$, $m_2 = 1M_\odot$, $a_1 = 10$AU and $a_2 = 100$AU. Eccentricities are initialized as $e_1 = 10^{-3}$ and $e_2 = 0.5$. Red lines: $i_{\rm tot} = 83^\circ$, $i_1 = 74.3^\circ$, $i_2 = 8.7^\circ$, $\omega_1 = 0^\circ$, $\Omega_1 = 0^\circ$; Blue lines: $i_{\rm tot} = 97^\circ$, $i_1 = 88^\circ$, $i_2 = 9^\circ$, $\omega_1 = 180^\circ$, $\Omega_1 = 180^\circ$.

$\Omega_{1,0} \to \Omega_{1,0} + \pi$). The evolution of eccentricity is indistinguishable between the prograde (red curves) and retrograde (blue curves) cases, while the inclination angle i_1 shows a reflection symmetry around 90°, evolving in an identical manner in both cases except for a phase offset of half of what can be interpreted as an "octupole period" (Teyssandier et al. 2013).

For the comparable-mass case ($m_1 \sim m_0$), the inner and outer binaries evolve together, exchanging angular momentum. Under reflection operation ($\mathbf{j}_1 \to -\mathbf{j}_1$), we find that $d\mathbf{j}_1/dt \to -d\mathbf{j}_1/dt$, $d\mathbf{e}_1/dt \to -d\mathbf{e}_1/dt$, $d\mathbf{j}_2/dt \to d\mathbf{j}_2/dt$ and $d\mathbf{e}_2/dt \to d\mathbf{e}_2/dt$, i.e., the symmetry of the equations is broken. Figure 2 shows the numerical integration in the case of general masses, for two configurations with similar reflection operation as in Figure 1. In this case, it is apparent that there is no reflection symmetry between the prograde (red curves) and retrograde (blue curves) initial conditions. Even the "octupole periods" are different.

3 EFFECTS OF SHORT-RANGE FORCES

The high eccentricity phase of a Lidov–Kozai cycle can be severely modified if the inner binary separation at pericenter is sufficiently small for additional forces to overcome the tidal torque exerted by the outer binary. If the energy associated to these extra forces $\Phi_{\rm extra}$ surpasses the interaction potential Φ of Equation (2), the Lidov–Kozai mechanism is said to be "arrested" (e.g. Wu & Murray 2003).

Here we study the effects of short-range forces on the eccentricity evolution of triple system consisting of a Jupiter-mass planet orbiting the primary star of a binary. The short range effects we consider include (1) precession of periapse due to GR, (2) tidal bulge of the planet induced by the star, and (3) planet oblateness due to rotation.

3.1 Conservative short-range forces

In the absence of energy dissipation (e.g., tidal friction or gravitational wave radiation), the energy of the system $\mathcal{H} = \mathcal{H}_1 + \mathcal{H}_2 + \Phi + \Phi_{\rm extra}$ is conserved, and so is its orbit-averaged version. Since the semimajor axes of the inner and outer orbits are constant, we only need to consider the conserved potential

$$\langle \Phi_{\rm tot} \rangle = \langle \Phi \rangle + \langle \Phi_{\rm GR} \rangle + \langle \Phi_{\rm Tide} \rangle + \langle \Phi_{\rm Rot} \rangle \ , \qquad (31)$$

where, as before, $\Phi = \Phi_{\rm Quad} + \Phi_{\rm Oct}$.

The post-Newtonian potential associated with periastron advance is (e.g., Eggleton & Kiseleva–Eggleton 2001)

$$\begin{aligned} \langle \Phi_{\rm GR} \rangle &= -\frac{3G^2 m_0 m_1 (m_0+m_1)}{a_1^2 c^2} \frac{1}{(1-e_1^2)^{1/2}} \\ &= -\varepsilon_{\rm GR} \mu_1 \Phi_0 \frac{1}{(1-e_1^2)^{1/2}} \ , \end{aligned} \qquad (32)$$

where we have defined the dimensionless parameter

$$\varepsilon_{\rm GR} \equiv \frac{3G(m_0+m_1)^2 a_2^3 (1-e_2^2)^{3/2}}{a_1^4 c^2 m_2} \ . \qquad (33)$$

The potential due to the non-dissipative tidal bulge on m_1 is

$$\begin{aligned} \langle \Phi_{\rm Tide} \rangle &= -\frac{G}{a_1^6} \frac{1+3e_1^2+\frac{3}{8}e_1^4}{(1-e_1^2)^{9/2}} \left(m_0^2 k_{2,1} R_1^5 \right) \\ &= -\varepsilon_{\rm Tide} \frac{\mu_1 \Phi_0}{15} \frac{1+3e_1^2+\frac{3}{8}e_1^4}{(1-e_1^2)^{9/2}} \ , \end{aligned} \qquad (34)$$

where

$$\varepsilon_{\rm Tide} \equiv \frac{15 m_0 (m_0+m_1) a_2^3 (1-e_2^2)^{3/2} k_{2,1} R_1^5}{a_1^8 m_1 m_2} \ , \qquad (35)$$

and $k_{2,1}$, R_1 are the tidal Love number and the radius of m_1, respectively. The potential energy associated with the rotation-induced oblateness of m_1 is

$$\langle \Phi_{\rm Rot} \rangle = -\frac{G m_0 (I_3 - I_1)_1}{2 a_1^3 (1-e_1^2)^{3/2}} \ . \qquad (36)$$

Here,

$$(I_3 - I_1)_1 = \frac{2}{3} k_{q,1} m_1 R_1^2 \left(\frac{\Omega_{1s}^2}{G m_1 / R_1^3} \right) \ , \qquad (37)$$

where $k_{q,1}$ is the apsidal motion constant and Ω_{1s} is the spin rate of m_1, and we have assumed that the spin vector of m_1 is aligned with the angular momentum vector $\mathbf{j}_1$ of the inner orbit. We can rewrite Equation (36) as

$$\langle \Phi_{\rm Rot} \rangle = -\varepsilon_{\rm Rot} \frac{\mu_1 \Phi_0}{3} \frac{1}{(1-e_1^2)^{3/2}} \ , \qquad (38)$$

where

$$\varepsilon_{\rm Rot} \equiv \frac{(m_0+m_1) a_2^3 (1-e_2^2)^{3/2} k_{q,1} \Omega_{1s}^2 R_1^5}{G a_1^5 m_1 m_2} \ . \qquad (39)$$

The three dimensionless parameters $\varepsilon_{\rm GR}$, $\varepsilon_{\rm Tide}$ and $\varepsilon_{\rm Rot}$ quantify the relative importance of the short-range potential terms respect to the quadrupole potential $\Phi_{\rm Quad}$.

Since the three short-range potentials (Equations 32, 34 and 38) depend on the orbital vectors solely through $e_1 = |\mathbf{e}_1|$, only the evolution equations for $\mathbf{e}_1$ is modified (see Equations 11 and 12). These extra forces induce an additional precession of $\mathbf{e}_1$ around $\mathbf{j}_1$:

$$\left.\frac{d\mathbf{e}_1}{dt}\right|_{\rm extra} = \dot{\omega}_{\rm extra}\ \hat{\mathbf{n}}_1 \times \mathbf{e}_1\ , \tag{40}$$

where (e.g., Fabrycky & Tremaine 2007).

$$\dot{\omega}_{\rm extra} = -\frac{\sqrt{1-e_1^2}}{e_1 L_1}\frac{\partial\langle\Phi_{\rm extra}\rangle}{\partial e_1}\ . \tag{41}$$

Thus, the GR-induced precession rate is:

$$\dot{\omega}_{\rm GR} = \frac{\varepsilon_{\rm GR}}{t_K}\frac{1}{1-e_1^2}\ . \tag{42}$$

Similarly, for the static tide, we have

$$\dot{\omega}_{\rm Tide} = \frac{\varepsilon_{\rm Tide}}{t_K}\frac{1+\frac{3}{2}e_1^2+\frac{1}{8}e_1^4}{(1-e_1^2)^5}\ , \tag{43}$$

and for the rotation-induced planet oblateness

$$\dot{\omega}_{\rm Rot} = \frac{\varepsilon_{\rm Rot}}{t_K}\frac{1}{(1-e_1^2)^2}\ . \tag{44}$$

To obtain an estimate of the relative importance of $\dot{\omega}_{\rm Tide}$ and $\dot{\omega}_{\rm Rot}$, we may consider a pseudo-synchronized planet spin, that is, the planet rotation rate Ω_{1s} is of order the orbital frequency of periapse $n_1(1-e_1^2)^{-3/2}$. In the weak friction theory of equilibrium tides, the pseudo-synchronized rotation rate is given by (e.g., Alexander 1973; Hut 1981)

$$\left(\frac{\Omega_{1s}}{n_1}\right)_{\rm ps} \equiv f_{\rm ps}(e_1) = \frac{1+\frac{15}{2}e_1^2+\frac{45}{8}e_1^4+\frac{5}{16}e_1^6}{1+3e_1^2+\frac{3}{8}e_1^4}\frac{1}{(1-e_1^2)^{3/2}}\ . \tag{45}$$

Thus, in Equation (44), we have $\varepsilon_{\rm Rot} = \varepsilon'_{\rm Rot} f_{\rm ps}^2(e_1)$ with

$$\varepsilon'_{\rm Rot} = \frac{(m_0+m_1)^2 a_2^3 (1-e_2^2)^{3/2} k_{q,1} R_1^5}{a_1^8 m_1 m_2}\ . \tag{46}$$

Comparing with $\dot{\omega}_{\rm Tide}$, we have $\dot{\omega}_{\rm Tide}/\dot{\omega}_{\rm Rot} \simeq (15 k_{2,1}/k_{q,1})$. Since $k_{2,1} \simeq 2k_{q,1}$, we find $\dot{\omega}_{\rm Tide} \gg \dot{\omega}_{\rm Rot}$ for synchronized rotation. Thus, in the vast majority of our examples, the effect of tides will dominate over the effect of the rotational bulge.

3.2 Numerical integrations

Before systematically examining the parameter space in $\varepsilon_{\rm Oct}$, $\varepsilon_{\rm GR}$, $\varepsilon_{\rm Tide}$ and $\varepsilon_{\rm Rot}$, we consider a few examples to illustrate how SRFs affect Lidov–Kozai oscillations.

In Figure 3, we show the evolution of a triple system with $\varepsilon_{\rm Oct} = 0.056$ and initial mutual inclination $i_{\rm tot} = 65^\circ$ obtained by numerical integration of the equations of motion in orbital elements form (see Appendix A). When SRFs are ignored (red curves), the inner orbit evolves into a highly eccentric state over a timescale of order $\varepsilon_{\rm Oct}^{-1} t_K$, reaching values as extreme as $1-e_1 < 10^{-5}$ (red curves, bottom panel). In this example, eccentricity maxima of $e_1 \to 1$ are always accompanied by orbital flips (red curves, top panel), i.e., the z-component of $\mathbf{j}$ reverses its sign. Orbital flips are always tied to eccentricity maxima and correspond to $\mathbf{j}_1$ shrinking going through the origin ($|\mathbf{j}_1| = 0$) as $e_1 \to 1$ (e.g., Katz, Dong, & Malhotra 2011). In some cases, it is possible to even derive a closed-form solution of this behaviour over long timescales provided the slowly varying quantity $\frac{4}{3}\Phi_{\rm Quad}/(\mu_1\Phi_0) - \frac{1}{2}(\mathbf{j}_1\cdot\hat{\mathbf{z}})^2 + \frac{1}{6}$ remains positive at all times (e.g., Katz, Dong, & Malhotra 2011). Assuming that the maximum eccentricity of a Lidov–Kozai cycle is reached when $j_z \equiv \mathbf{j}_1\cdot\hat{\mathbf{z}}$ crosses zero, Katz, Dong, & Malhotra (2011) find that the maximum e_1 scales with $\varepsilon_{\rm Oct}$ roughly as $\sim\sqrt{1-\varepsilon_{\rm Oct}^2}$. If this theoretical maximum cannot be reached owing to additional effects such as SRFs, then we expect that j_z will be unable to come arbitrarily close to zero, and therefore orbital flips will not be allowed.

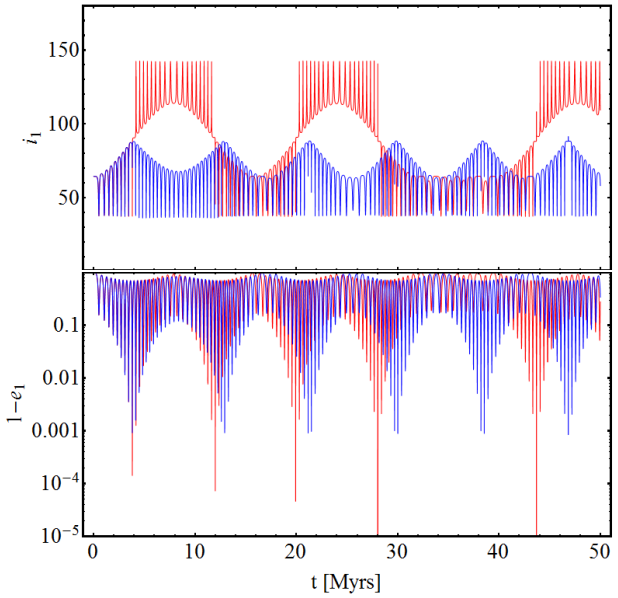

Figure 3. Numerical integration of a system with parameters $m_0 = 1M_\odot$, $m_1 = 1M_J$, $m_2 = 40M_J$ $a_1 = 6$AU and $a_2 = 100$AU. Initial conditions are $e_1 = 0.001$, $e_2 = 0.6$, $i_1 = 64.7^\circ$, $i_2 = 0.3^\circ$, $i_{\rm tot} = 65^\circ$, $\omega_1 = 45^\circ$, $\omega_2 = 0^\circ$, $\Omega_1 = 0^\circ$ and $\Omega_2 = 180^\circ$. Total integration time is 50 Myr$\sim 360 t_K$. The red lines are from the integration of the pure Lidov–Kozai effect to octupole order, while the blue lines are the results of integration including SRFs. Orbital flips seem to be entirely suppressed. However, when extending the integration time to ~ 300 Myrs $\sim 2100 t_K$, the inner orbit eventually flips to retrograde in the interval of 90–130 Myr before going back to its original orientation.

Indeed, when SRFs are included (blue curves), the maximum eccentricity is capped down to values such that $1-e_1 \simeq 10^{-3}$ (blue curves, bottom panel). Although still large, this upper limit to the eccentricity is sufficient to introduce a lower limit to $|\mathbf{j}_1|$ (see Section 3.3 below) such that j_z cannot reverse signs under the criterion introduced by Katz, Dong, & Malhotra (2011). As a result, we see no orbital flips in this example (red curves, top panel).

Surprisingly, however, orbital flips are not prohibited in every case. In Figure 4, we present an example of a system which exhibits an orbital flip even though the maximum allowed eccentricity has been reduced by SRFs. As in the previous example, we integrate a triple system with $\varepsilon_{\rm Oct} = 0.056$ with and without SRFs (blue and red curves

respectively). This time, the initial conditions are modified slightly, changing the initial mutual inclination angle from $i_{\rm tot} = 65^\circ$ to $i_{\rm tot} = 65.3783^\circ$. Over the first half of the integration, the evolution of eccentricity (bottom panel) and inclination (top panel) in Figure 4 closely resemble of those of Figure 3. However, after 25 Myrs, the two systems start following entirely differently trajectories, despite the very small difference in initial conditions. In addition, the figure shows that this system finds a way to cause an orbital flip (i.e. j_z crosses zero), despite that the eccentricity is not allowed to exceed $e_1 = 1 - 10^{-3}$ just as in Figure 3. From Figure 4, we conclude that (1) orbital flips can still take place in presence of SFRs that are strong enough to limit the eccentricity maximum, and (2) that the inclination of the inner binary may exhibit chaotic behaviour (e.g. Li et al. 2014b), and that conservative SRFs modify do not necessarily suppress this erratic evolution. To check whether the example of Figure 3 has entirely suppressed orbital flips or if it is just a matter of time before it finds a channel to cross $j_z = 0$, we integrate the system for 300 Myr $\sim 2100 t_K$. Indeed, we confirm that after a very long time $\sim 500 t_K$, this system also undergoes an orbital flip that lasts for $300 t_K$ before returning to its original orientation.

Figure 5 shows the evolution of j_z and the angle $\Omega_e \equiv \arctan(e_y/e_x)$ (see Katz, Dong, & Malhotra 2011) for the example of Figure 4. The red curves show the evolution of the system in the absence of SRFs, where a regular oscillation of j_z at earlier times transitions to a different regime after ~ 35 Myrs. When SRFs are included (blue curves), the evolution of j_z stays bounded between its initial value and zero, without being allowed to change sign, until suddenly a flip takes place. The transition between these two regimes can be seen in the evolution of Ω_e (bottom panel). At early times, Ω_e remains bounded between -100° and $+100^\circ$. However, by the time j_z changes sign, Ω_e is circulating, sweeping all possible angles. An analogous plot of Ω_e for the example in Figure 3 shows that Ω_e never circulates during the entire extent of the integration.

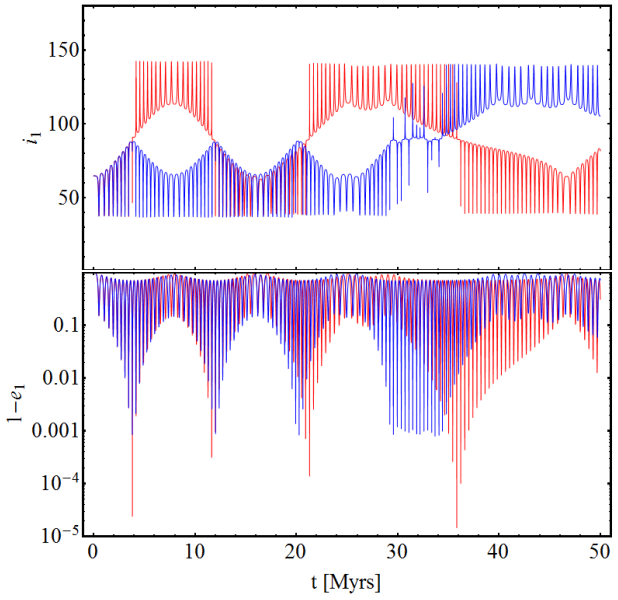

Figure 4. Same initial conditions as in Figure 3, but slightly changing the initial inclination: $i_{\rm tot} = 65.3783^\circ$ with $i_1 = 64.9734^\circ$ and $i_2 = 0.4049^\circ$.

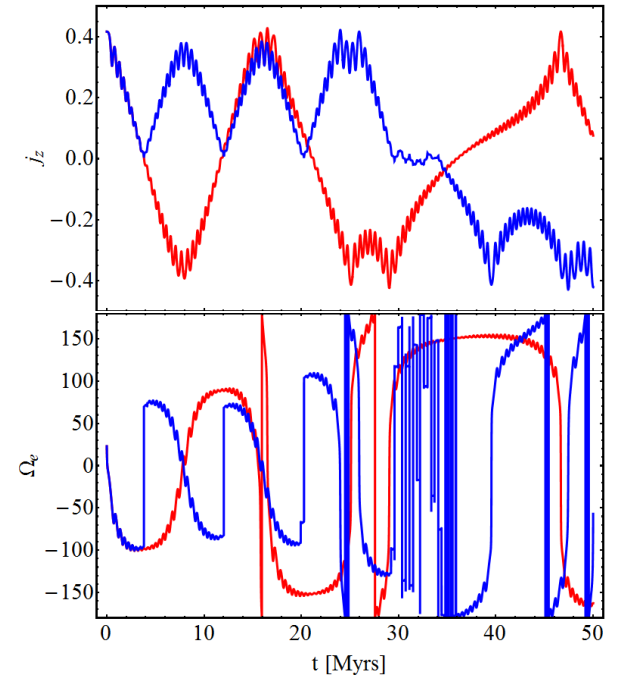

Figure 5. Evolution of $j_z = \mathbf{j}_1 \cdot \hat{\mathbf{z}}$ and $\Omega_e \equiv \arctan(e_y/e_x)$ for the case corresponding to Figure 4. The red lines are from the integration of pure Lidov–Kozai effect in octupole order, while the blue lines are the results of integration including SRFs. When SRFs limit the maximum eccentricity, flips are suppressed if Ω_e is bounded, but they become possible once again if Ω_e is circulating.

3.3 Maximum eccentricity: analytical results

We see in Section 3.2 that SRFs limit the maximum eccentricity that can be achieved during the Lidov–Kozai cycles (e.g., Holman, Touma, & Tremaine 1997; Fabrycky & Tremaine 2007). In the test-mass approximation ($m_1 \ll m_0$) and neglecting the octupole effect, this maximum eccentricity, $e_{1,\rm max}$, can be derived analytically. We shall see in Section 4 that the limiting eccentricity, $e_{\rm lim}$, achieved for the initial inclination $i_0 = 90^\circ$, is also applicable when the octupole effect is included and binaries of comparable masses ($m_1 \sim m_0$) are considered.

In the test-mass approximation ($m_1 \ll m_0$, which implies $d\mathbf{j}_2/dt = d\mathbf{e}_2/dt = 0$) and at the quadrupole level ($\varepsilon_{\rm Oct} = 0$), Equation (17) implies

$$\mathbf{j}_1 \cdot \hat{\mathbf{n}}_2 = \sqrt{1-e_1^2}\cos i_1 = \text{constant} \quad . \tag{47}$$

In addition, the total potential is conserved

$$\langle \Phi_{\rm tot} \rangle \approx \langle \Phi_{\rm Quad} \rangle + \langle \Phi_{\rm GR} \rangle + \langle \Phi_{\rm Tide} \rangle + \langle \Phi_{\rm Rot} \rangle = \text{constant} \quad . \tag{48}$$

In terms of the orbital elements of the inner binary, the

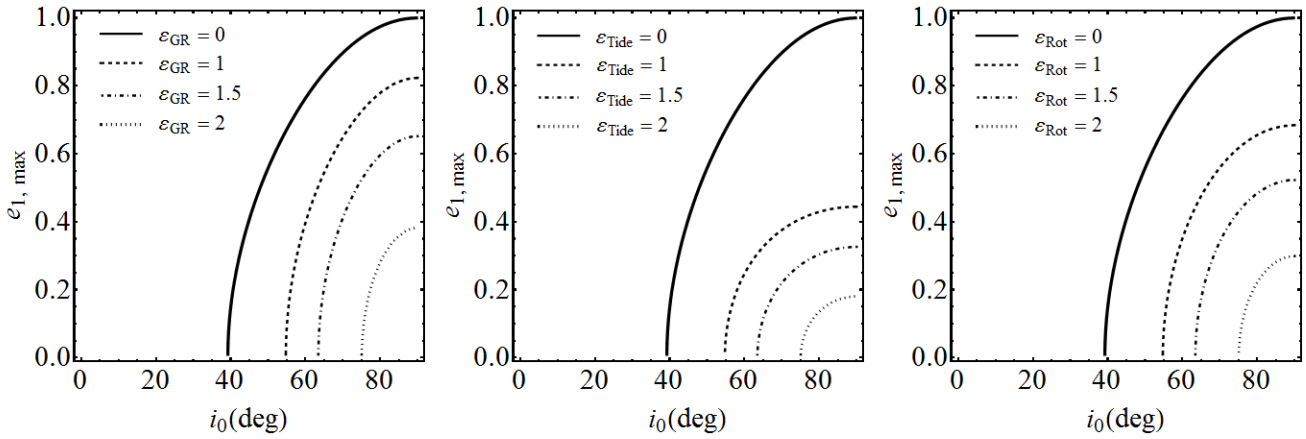

Figure 6. The maximum eccentricity of the inner binary (when $m_1 \ll m_0$) as a function the initial inclination i_0 for different values of $\varepsilon_{\rm GR}$, $\varepsilon_{\rm Tide}$, $\varepsilon_{\rm Rot}$. In these illustrative examples, SRFs compete with Lidov-Kozai oscillations from the start (when $e_{1,0} \sim 0$); however, for more realistic parameters (see Section 4 below), SRFs only dominate over the tidal potential Φ when $e_1 \sim 1$ (see values of $\varepsilon_{\rm extra}$ in Table 1).

quadrupole potential (Equation 7) can be written as

$$\langle \Phi_{\rm Quad} \rangle = -\frac{\mu_1 \Phi_0}{8}\Big[2{+}3e_1^2{-}(3{+}12e_1^2{-}15e_1^2\cos^2\omega_1)\sin^2 i_{\rm tot}\Big], \tag{49}$$

If the system is initialized with $e_1 = 0$, the maximum eccentricity $e_{1,\rm max}$ is achieved at $\omega_1 = \pi/2$ or $3\pi/2$ during the Lidov–Kozai cycles. Using Equations (47) (49), we find that $e_{1,\rm max}$ is given by

$$\varepsilon_{\rm GR}\left(\frac{1}{j_{1,\rm min}}-1\right)+\frac{\varepsilon_{\rm Tide}}{15}\left(\frac{1+3e_{1,\rm max}^2+\frac{3}{8}e_{1,\rm max}^4}{j_{1,\rm min}^9}-1\right) + \frac{\varepsilon_{\rm Rot}}{3}\left(\frac{1}{j_{1,\rm min}^3}-1\right)=\frac{9}{8}\frac{e_{1,\rm max}^2}{j_{1,\rm min}^2}\left(j_{1,\rm min}^2-\frac{5}{3}\cos^2 i_0\right), \tag{50}$$

where $j_{1,\rm min} = \sqrt{1-e_{1,\rm max}^2}$. In the absence of the SRFs ($\varepsilon_{\rm GR} = \varepsilon_{\rm Tide} = \varepsilon_{\rm Rot} = 0$), the above equation yields the well-known maximum eccentricity $e_{\rm m0}$ for "pure" Lidov–Kozai oscillation (e.g., Kozai 1962; Lidov 1962)

$$e_{\rm m0} = \sqrt{1-\frac{5}{3}\cos^2 i_0}\ , \tag{51}$$

If we neglect the tidal or rotation terms ($\varepsilon_{\rm Tide} = \varepsilon_{\rm Rot} = 0$) and assume $\varepsilon_{\rm GR} \ll 1$, Equation (50) results to (e.g., Miller & Hamilton 2002)

$$j_{1,\rm min} = \frac{1}{9}\Big[4\varepsilon_{\rm GR}+\sqrt{16\varepsilon_{\rm GR}^2+135\cos^2 i_0}\Big] \tag{52}$$

Figure 6 depicts several example of $e_{1,\rm max}$ for different values of $\varepsilon_{\rm GR}$, $\varepsilon_{\rm Tide}$, $\varepsilon_{\rm Rot}$.

The physical meaning of Equation (50) can be made clear if we use the expression of $\dot\omega_{\rm extra}$ Equations 42–44) to re-express it as (assuming $j_{1,\rm min} \ll 1$)

$$\left[\frac{\dot\omega_{\rm GR}}{\dot\omega_K}+\frac{1}{15}\frac{\dot\omega_{\rm Tide}}{\dot\omega_K}f(e_1)+\frac{1}{3}\frac{\dot\omega_{\rm Rot}}{\dot\omega_K}\right]_{e_1=e_{1,\rm max}} \approx \frac{9}{8}e_{1,\rm max}^2\frac{j_{1,\rm min}^2-5\cos^2 i_0/3}{j_{1,\rm min}^2}\ , \tag{53}$$

where

$$f(e_1) \equiv \frac{1+3e_1^2+\frac{3}{8}e_1^4}{1+\frac{3}{2}e_1^2+\frac{1}{8}e_1^4}\ , \tag{54}$$

and where we have defined for convenience a "characteristic" Lidov–Kozai rate

$$\dot\omega_K \equiv \frac{1}{t_K\sqrt{1-e_1^2}}\ , \tag{55}$$

which should not be confused with the precession rate derived from applying the operation in Equation 41 to $\langle \Phi_{\rm Quad}\rangle$.

For $i_0 = 90^\circ$, the eccentricity attains the limiting value, $e_{\rm lim} \equiv e_{1,\rm max}$, given by

$$\left[\frac{\dot\omega_{\rm GR}}{\dot\omega_K}+\frac{1}{15}\frac{\dot\omega_{\rm Tide}}{\dot\omega_K}f(e_1)+\frac{1}{3}\frac{\dot\omega_{\rm Rot}}{\dot\omega_K}\right]_{e_1=e_{\rm lim}} = \frac{9}{8}e_{\rm lim}^2\ . \tag{56}$$

For $1-e_{\rm lim} \ll 1$, we have $f(e_{\rm lim}) \simeq 5/3$, Equation (56) becomes

$$\left[\frac{\dot\omega_{\rm GR}}{\dot\omega_K}+\frac{1}{9}\frac{\dot\omega_{\rm Tide}}{\dot\omega_K}+\frac{1}{3}\frac{\dot\omega_{\rm Rot}}{\dot\omega_K}\right]_{e_1=e_{\rm lim}} \simeq \frac{9}{8}\ . \tag{57}$$

Thus, the limiting eccentricity is achieved when the periapse precession rate due to SRFs becomes comparable to the Lidov–Kozai rate $\dot\omega_K$.

4 PARAMETER SURVEY: TEST-MASS CASES

In the test-mass limit ($m_1 \ll m_0$), the evolution of the inner binary depends on the dimensionless ratios $\varepsilon_{\rm Oct}$, $\varepsilon_{\rm GR}$, $\varepsilon_{\rm Tide}$, $\varepsilon_{\rm Rot}$ as well as the initial inclination angle i_0 (we assume $e_0 \simeq 0$). In this section, we consider the evolution of Jupiter-mass planet ($m_1 = m_J, R_1 = R_J$) moving around a Solar-mass star ($m_0 = m_\odot$). We carry out calculations for different values of a_1, a_2, m_2 and e_2. The different orbital configurations and their corresponding values of $\varepsilon_{\rm Oct}$ and $\varepsilon_{\rm extra}$ are listed in Table 1. These conditions of parameters are subject to the stability criterion of Mardling & Aarseth (2001)

$$\frac{a_2}{a_1} > 2.8\left(1+\frac{m_2}{m_0}\right)^{2/5}\frac{(1+e_2)^{2/5}}{(1-e_2)^{6/5}}\left(1-\frac{0.3i_{\rm tot}}{180^\circ}\right)\ . \tag{58}$$

Table 1. Initial conditions on different cases: $m_0 = 1M_\odot$, $m_1 = 1M_J$, $e_0 = 0.001$, $k_{2,1} = 0.37$, $k_{q,1} = 0.17$, $R_1 = 1R_J$, $\omega_1 = \omega_2 = \Omega_1 = 0°$ and $\Omega_2 = 180°$. The parameter $\varepsilon_{\rm extra}$ is calculated by definition in Equations (33), (35) and (39).

Parameter	$\varepsilon_{\rm Oct}$	$\varepsilon_{\rm GR}$	$\varepsilon_{\rm Tide}$	a_1(AU)	a_2(AU)	e_2	$m_2(M_\odot)$
Case 1	0.001	4.47×10^{-1}	2.61×10^{-6}	1	200	0.2	0.5
Case 2	0.002	2.79×10^{-2}	1.63×10^{-7}	1	100	0.2	1
Case 3a	0.006	1.72×10^{-4}	7.78×10^{-13}	6	200	0.2	1
Case 3b	0.006	1.03×10^{-3}	6.05×10^{-9}	1	33.33	0.2	1
Case 3c	0.006	1.03×10^{-2}	6.05×10^{-8}	1	33.33	0.2	0.1
Case 4	0.011	5.13×10^{-2}	3.00×10^{-7}	1	200	0.8	1
Case 5	0.013	2.15×10^{-5}	9.72×10^{-14}	6	100	0.2	1
Case 6	0.022	6.41×10^{-3}	3.75×10^{-8}	1	100	0.8	1
Case 7	0.033	3.08×10^{-5}	2.89×10^{-13}	5	100	0.5	1
Case 8	0.044	4.01×10^{-4}	1.46×10^{-10}	2	100	0.8	1
Case 9	0.056	2.93×10^{-4}	1.32×10^{-12}	6	100	0.6	0.04
Case 10a	0.067	3.96×10^{-5}	1.79×10^{-13}	6	200	0.8	1
Case 10b	0.067	2.37×10^{-4}	1.39×10^{-9}	1	33.33	0.8	1
Case 10c	0.067	2.37×10^{-3}	1.39×10^{-8}	1	33.33	0.8	0.1
Case 11	0.133	4.95×10^{-6}	2.23×10^{-14}	6	100	0.8	1

Table 2. Results for the different cases listed in Table 1. The limiting eccentricity $e_{\rm lim}$ is obtained from Equation (56) in the case of $i_0 = 90°$ and pseudo synchronized. $e_{\rm max,Num}$ means the maximum eccentricity found from the numerical integration's results. We also define three angles: $i_0|^{\rm SRF}_{e\rm lim}$ is the initial inclination where the simulation result $e_{\rm max}$ first reaches the analytic value $e_{\rm lim}$, $i_0|_{\rm flip}$ is the smallest angle at which the first flipping orbit occurs without tidal friction and $i_0|^{\rm SRF}_{\rm flip}$ is the one with SRFs.

Parameter	$1-e_{\rm lim}$	$1-e_{\rm max,Num}$	$\frac{\dot\omega_{\rm GR}}{\omega_{\rm K}}\big\vert_{e_{\rm lim}}$	$\frac{\dot\omega_{\rm Tide}}{\omega_{\rm K}}\big\vert_{e_{\rm lim}}$	$\frac{\dot\omega_{\rm Rot}}{\omega_{\rm K}}\big\vert_{e_{\rm lim}}$	$i_0\,\vert_{\rm flip}$(deg)	$i_0\,\vert^{\rm SRF}_{\rm flip}$(deg)	$i_0\,\vert^{\rm SRF}_{e\rm lim}$(deg)
Case 1	5.01×10^{-2}	4.92×10^{-2}	1.43	2.24×10^{-1}	2.76×10^{-2}	87.7	~ 90	88.5
Case 2	1.28×10^{-2}	1.11×10^{-2}	1.75×10^{-1}	6.23	7.85×10^{-1}	86.2	~ 90	85.4
Case 3a	8.12×10^{-4}	7.00×10^{-4}	4.28×10^{-3}	7.29	9.27×10^{-1}	82.2	~ 90	87.1
Case 3b	5.97×10^{-3}	5.16×10^{-3}	9.48×10^{-3}	7.21	9.13×10^{-1}	82.2	~ 90	86.8
Case 3c	1.01×10^{-2}	8.71×10^{-3}	7.30×10^{-2}	6.81	8.60×10^{-1}	82.2	~ 90	85.4
Case 4	1.51×10^{-2}	1.31×10^{-4}	2.91×10^{-1}	5.56	7.00×10^{-1}	80.2	~ 90	83.9
Case 5	5.11×10^{-4}	4.41×10^{-4}	6.74×10^{-4}	7.32	9.31×10^{-1}	79.0	89.4	78.8
Case 6	9.02×10^{-3}	7.78×10^{-3}	4.78×10^{-2}	6.96	8.80×10^{-1}	69.9	89.1	71.9
Case 7	6.51×10^{-4}	5.51×10^{-4}	8.55×10^{-4}	7.32	9.30×10^{-1}	58.7	60.4	59.3
Case 8	2.60×10^{-3}	2.23×10^{-3}	5.55×10^{-3}	7.27	9.23×10^{-1}	51.3	73.3	51.9
Case 9	9.14×10^{-4}	7.71×10^{-4}	6.86×10^{-3}	7.28	9.25×10^{-1}	47.8	56.0	49.1
Case 10a	5.85×10^{-4}	4.91×10^{-4}	1.16×10^{-3}	7.31	9.30×10^{-1}	47.3	53.9	47.8
Case 10b	4.29×10^{-3}	3.67×10^{-3}	2.56×10^{-3}	7.27	9.22×10^{-1}	47.3	73.1	51.9
Case 10c	7.19×10^{-3}	6.15×10^{-3}	1.98×10^{-2}	7.14	9.03×10^{-1}	47.3	81.1	52.1
Case 11	3.68×10^{-4}	3.09×10^{-4}	1.82×10^{-4}	7.32	9.31×10^{-1}	47.3	48.4	49.6

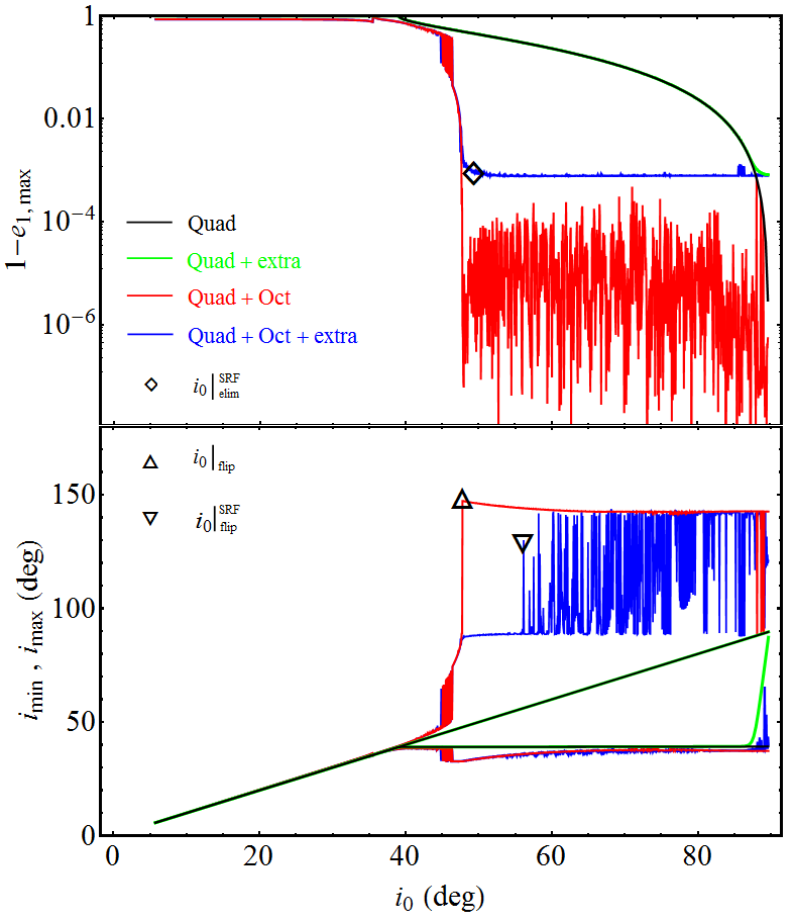

Figure 7. Case 9 in Table 1 with $\varepsilon_{\rm Oct} = 0.056$. Same values of m_0, m_1, m_2, a_1, a_2 and e_2 from Figures 3 and 4, extending initial mutual inclination to the full range $(0°, 90°)$ (in all cases, $\omega_1 = 0°$, $\omega_2 = 0°$, $\Omega_1 = 0°$ and $\Omega_2 = 180°$ at $t = 0$). We integrate Equations (A1)-(A7) for quadrupole ($\varepsilon_{\rm Oct} = 0$) and octupole ($\varepsilon_{\rm Oct} \neq 0$) approximations of the potential as well as without ($\varepsilon_{\rm extra} = 0$) and with ($\varepsilon_{\rm extra} \neq 0$) SRFs. The total integration time is 5×10^7 years ($\sim 360.5\ t_K$). The upper panel shows the maximum eccentricity $e_{1,\max}$ achieved over the entire integration time for the four different approximation used. Similarly, the lower panel shows the extrema in inclination $i_{0,\max/\min}$ attained during the evolution. Black curves correspond to "pure" quadrupole-level Lidov–Kozai oscillations (i.e., $\varepsilon_{\rm Oct} = 0$ and $\varepsilon_{\rm extra} = 0$); green curves correspond to quadrupole-level Lidov–Kozai oscillations *with* SRFs ($\varepsilon_{\rm Oct} = 0$ and $\varepsilon_{\rm extra} \neq 0$); red curves correspond to "pure" octupole-level Lidov–Kozai oscillations ($\varepsilon_{\rm Oct} \neq 0$ and $\varepsilon_{\rm extra} = 0$); and blue curves correspond to octupole-level Lidov–Kozai oscillations with SRFs ($\varepsilon_{\rm Oct} \neq 0$ and $\varepsilon_{\rm extra} \neq 0$). Blue curves show how strict SRFs are in establishing a global maximum eccentricity, capping the octupole-level evolution at the limiting value $e_{\rm lim}$ given by Equation 56. Inclination is strongly affected by the octupole terms even in the presence of SRFs, however flips are suppressed i_0 below 60°, limiting those orbits to a maximum inclination of 90°, but not beyond that value. Triangular and square markers denote different transitions in the behaviour of e_1 and i_1 (see text and Table 2).

For each combination of $\varepsilon_{\rm Oct}$ and $\varepsilon_{\rm extra}$ (Table 1), we integrate a total of 300 triple systems over a total integration time ranging from $\sim 360 t_K$ to $\sim 500 t_K$. We setup each system by varying the initial inclination of the inner binary i_0 ($\simeq i_{\rm tot,0}$ when $m_1 \ll m_0$) between 0° and 90°.

4.1 A fiducial example with $\varepsilon_{\rm Oct} = 0.056$

We first consider a specific example with $\varepsilon_{\rm Oct} = 0.056$ (Case 9 in Table 1). For each initial inclination angle i_0 (in the range between 0° and 90°), we integrate Equations (A1)-(A7) for 5×10^7 yrs, corresponding to $360.5\ t_K \sim 10 t_K/\varepsilon_{\rm Oct}$ for this specific set of parameters. For each of these subsystems, we record the maximum eccentricity $e_{1,\max}$ and the maximum and minimum of $i_{\rm tot}$ attained during the evolution. The results are shown in Figure 7.

4.1.1 Eccentricity maxima

The upper panel in Figure 7 shows the maximum eccentricity of inner orbit as a function of i_0. At the quadrupole level, the pure Lidov–Kozai cycles can give extremely large eccentricity ($1 - e_{1,\max} \leqslant 10^{-5}$) only for $i_0 \simeq 90°$. When the short-range effects are included, the value of $e_{1,\max}$ at that point is limited to $1 - e_{1,\max} \leqslant 10^{-3}$, in accordance with the analytic expression (Equation 50). For the parameters considered in this case (Case 9), the tidal effect plays the dominate role in limiting the maximum eccentricity (Table

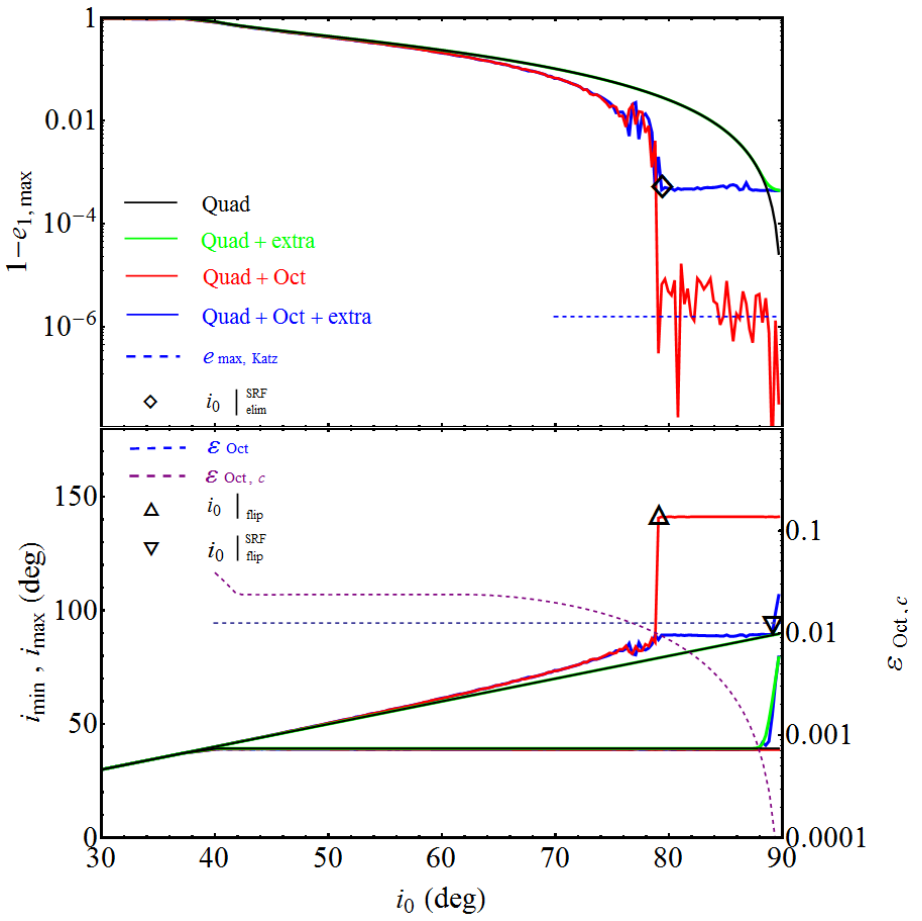

Figure 8. Same as Figure 7, but now corresponding to Case 5 in Table 1. ($\varepsilon_{\rm Oct} = 0.013$). We integrate the Equations for 5×10^6 years ($\sim 490.6\ t_K$). System parameters are $m_0 = 1M_\odot$, $m_1 = 1M_J$, $m_2 = 1M_\odot$, $a_1 = 6$AU and $a_2 = 100$AU. We start each run with $e_1 = 0.001$, $e_2 = 0.2$, $\omega_1 = 0°$, $\omega_2 = 0°$, $\Omega_1 = 0°$ and $\Omega_2 = 180°$. Qualitative behaviour of this set of systems is similar to that of Figure 7, except that now the "window of influence" of octupole effects is much narrower, limiting the importance of octupolar corrections and enabling SRFs to severely limit their resulting extreme orbits. In particular, although octupole terms can still alter inclinations beyond the quadrupole-level predictions, in this example orbital flips have been entirely suppressed. Dashed lines correspond to the estimates provided by Katz, Dong, & Malhotra (2011) for the maximum eccentricity $e_{\rm max,Katz}$ within the "window of influence" (upper panel) and for the critical value $\varepsilon_{{\rm Oct},c}$ above which orbital flips are allowed (see Section 4.3).

2, when we see that $\dot\omega_{\rm Tide}/(9\dot\omega_K) \gg \dot\omega_{\rm Rot}/(3\dot\omega_K) \gg \dot\omega_{\rm GR}/\dot\omega_K$ at $e_1 = e_{\rm lim}$; see also Equation 57).

When the octupole term is included, there is a sharp jump of $e_{1,max}$ at $i_0 \approx 50°$. Without the SRFs, $(1 - e_{\rm max})$ becomes very small and varies erratically as i_0 increases beyond 50°. This erratic variation is the result of the overlap between the quadrupole and octupole contributions. When the SRFs are included, we find that instead of the rapid variation of $(1 - e_{\rm max})$, the maximum eccentricity becomes approximately a constant, equal to $e_{\rm lim}$. We define $i_0|^{\rm SRF}_{\rm elim}$ as the the value of i_0 when $e_{\rm max}$ first reaches $e_{\rm lim}$. For the case considered in Fig. 7, $i_0|^{\rm SRF}_{\rm elim}$ is close to 50°. It is important to note that although $e_{\rm lim}$ is derived in the quadrupole approximation (see Section 3.3), it serves as the maximum eccentricity attainable even when the octupole term is included.

4.1.2 Inclination extrema

The lower panel in Figure 7 shows the maximum and minimum of the orbital inclination attained during the evolution of the inner binary as functions of i_0. At the pure quadrupole level (without SRFs), the inclination does not change until i_0 reaches $\arccos\sqrt{3/5} \simeq 40°$, beyond which $i_{\rm max} = i_0$ and $i_{\rm min} = 40°$. Including SRFs, $i_{\rm min}$ is modified for i_0 close to 90° as the maximum eccenticity is limited by the SRFs. Note that $\sqrt{1-e^2_{\rm max}}\cos i_{\rm min} = \cos i_0$.

At the octupole level, the angular momentum of the inner binary experiences a flip ($i_{\rm max} > 90°$) at a critical angle $i_0|_{\rm flip}$. This angle is always greater than 40° (the onset of quadrupole Lidov–Kozai oscillations). When the SRFs are included, this critical angle is pushed to a higher value, $i_0|^{\rm SRF}_{\rm flip}$.

At inclinations slightly higher than the angle critical $i_0|^{\rm SRF}_{\rm elim}$ (demarcated by inverted triangle in Figure 7, the orbital flips seen in absence of SRFs (red curves) have now been inhibited. Note, however, that at even higher inclina-

tions ($i_0 > i_0|_{\rm flip}^{\rm SRF}$), orbital flips are once again allowed. This can occur even though the maximum eccentricity $e_{1,\rm max}$ is strongly affected by the SRFs (see Figure 5 and Section 3.2). Note also that the individual examples shown in Figures 4 and 5 (with i_0 of 65° and 65.3783° respectively) lie within the erratically varying region that starts at $i_0|_{\rm flip}^{\rm SRF} \sim 56°$. It is possible that the inclination angle in the example with $i_0 = 65°$ (Figure 4) will eventually flip as well. From this figure we can conclude that SRFs have broken the symmetry that existed between the upper and lower panels of Figure 7 (red curves), which showed that both the extreme maximum eccentricity and the orbital flip where achieved above the same critical inclination.

The erratic variation of $i_{\rm max}$ for $i_0 > i_0|_{\rm flip}^{\rm SRF}$ results from the combined effects of quadrupole, octupole and SRFs, and may be associated with the chaotic behaviour of Lidov–Kozai oscillations studied by Li et al. (2014b). These authors find that configurations with higher inclinations and larger $\varepsilon_{\rm Oct}$ are more chaotic (with Lyapunov times of $\sim 6t_K$ for the chaotic regions of parameter space). It is possible that the complexity of a system with conservative SRFs (three additional frequencies are present and no energy dissipation) only shift the inclination threshold for chaotic behaviour to larger angles, but have not fundamentally suppressed the chaotic nature of Lidov–Kozai oscillations with octupole-level terms. It is also possible that the characteristic timescale for a flip has been entirely altered by the SRFs, and that all systems with $i_0 > i_0|_{\rm flip}^{\rm SRF}$ will eventually flip (on timescales much longer than $t_K/\varepsilon_{\rm Oct}$).

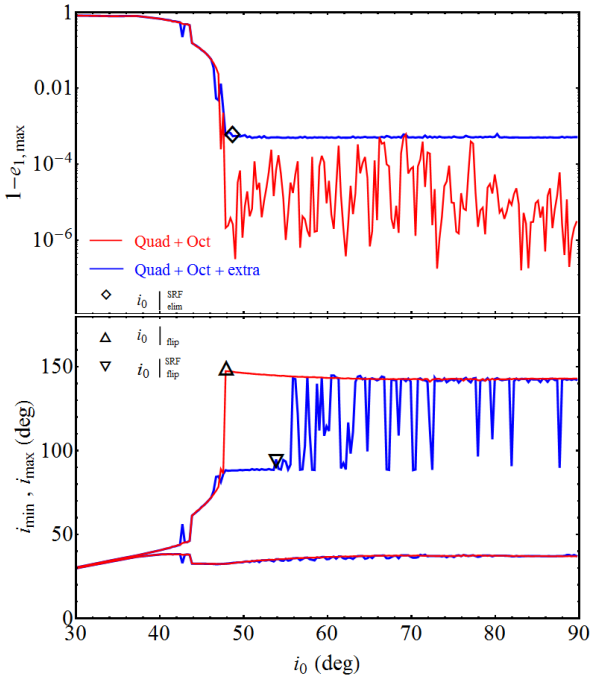

Figure 9. Case 10a in Table 1 ($\varepsilon_{\rm Oct} = 0.067$, $\varepsilon_{\rm GR} = 3.96 \times 10^{-5}$, $\varepsilon_{\rm Tide} = 1.79 \times 10^{-13}$). System parameters are $m_0 = 1M_\odot$, $m_1 = 1M_J$, $m_2 = 1M_\odot$ $a_1 = 6$AU and $a_2 = 200$AU. Orbits are started with $e_1 = 0.001$, $e_2 = 0.8$, $\omega_1 = 0°$, $\omega_2 = 0°$, $\Omega_1 = 0°$ and $\Omega_2 = 180°$. The total integration time is 6×10^6 years ($\sim 320.5\ t_K$).

4.2 Dependence of $e_{1,\rm max}$ and $i_0|_{\rm flip}$ with $\varepsilon_{\rm Oct}$

To explore how the extrema in e_1 and i_1 change with i_0 for different values of $\varepsilon_{\rm Oct}$, we carry out another set of numerical integrations, this time with $\varepsilon_{\rm Oct} = 0.013$ (listed as 'Case 5' in Table 1 below). The results of this set of integrations are shown in Figure 8. Without SRFs (red curves), the $e_{1,\rm max}$ and $i_{\rm min/max}$ curves exhibit the same overall morphology observed in the case with $\varepsilon_{\rm Oct} = 0.056$ (Figure 7). In this case, however, significant deviations from the quadrupole-only calculations are confined to a narrower range in i_0. This is to be expected, since this "octupole active" region will gradually shrink as $\varepsilon_{\rm Oct}$ is made smaller, until the quadrupole level solutions (black and green curves) are recovered. In the limit $\varepsilon_{\rm Oct} \to 0$, the only angle which allows for $e_{1,\rm max} = 1$ is $i_0 = 90°$ (Equation 51). Similarly, when $\varepsilon_{\rm Oct} \to 0$ only $i_0 = 90°$ permits $j_z = 0$.

Quantitatively, the width along the i_0-axis of the octupole-active region or "window of influence" for a given value of $\varepsilon_{\rm Oct}$ can be understood using the "flip condition" identified by Katz, Dong, & Malhotra (2011). From approximate conservation laws, these authors find that, given $e_{1,0} \sim 0$ and $j_{z,0} \sim \cos i_0$, the long term oscillation of j_z owing to octupole terms can only result in a change of sign if and only if i_0 is greater than a critical value that depends on $\varepsilon_{\rm Oct}$. Equivalently, given i_0, there is a critical value $\varepsilon_{\rm Oct,c}$ above which orbits will flip. This flip condition can be approximately expressed as $\varepsilon_{\rm Oct,c} = \frac{1}{2}F(\cos^2 i_0/2)$ where $F(x)$ is a non-monotonic function that is equal to zero at $x = 0$ and $x \approx 0.236$ and peaks at 0.0475 for $x \approx 0.112$ (see Katz, Dong, & Malhotra 2011, Eqs. 17). The critical value $\varepsilon_{\rm Oct,c}$ is a monotonically decreasing function of i_0, meaning that the closer i_0 is to 90°, the smaller $\epsilon_{\rm Oct,c}$ becomes (i.e., the easier it is to flip). We illustrate this by overlaying $\epsilon_{\rm Oct,c}$ as a function of i_0 in the bottom panel of Figure 8. When $\epsilon_{\rm Oct,c}$ becomes smaller than $\varepsilon_{\rm Oct} = 0.013$ (at $i_0 \sim 77°$), test particle trajectories are allowed to flip orientations. Above this critical angle, each orbital flip is accompanied by an extreme increase in eccentricity. Following Katz, Dong, & Malhotra (2011), we estimate that this limiting eccentricity within the octupole active region is such that $1 - e_{\rm max,Katz}^2 \approx (0.14\ \varepsilon_{\rm Oct})^2$, i.e., $1 - e_{\rm max,Katz} \approx 1.7 \times 10^{-6}$, which is in good agreement with the average value of $e_{1,\rm max}$ in the region where $i_0 > 79°$.

When SRFs are included, (blue and green curves in Figure 8), the modifications to the evolution of eccentricity are consistent with what was observed in the $\varepsilon_{\rm Oct} = 0.056$ example. However, the amplitude of the inclination oscillations is more dramatically affected. On one hand, we find a consistently truncated maximum eccentricity down to a value of $1 - e_{1,\rm max} \approx 4.41 \times 10^{-4}$, in rough agreement with the value of $1 - e_{\rm lim} \approx 5.11 \times 10^{-4}$ predicted by Equation (56). On the other hand, the orbital flips above $i_0 \sim 79°$ are entirely suppressed, in contrast with the behaviour observed in Figure 7, where only a fraction of the systems have their orbital flips entirely suppressed, while at high inclinations the orbits still manage to reverse their orientations despite the strict limits on the maximum eccentricity.

4.3 Parameter space

We have carried out calculations of the inner binary evolution for various combinations of a_1, a_2, m_2, e_2 that yield

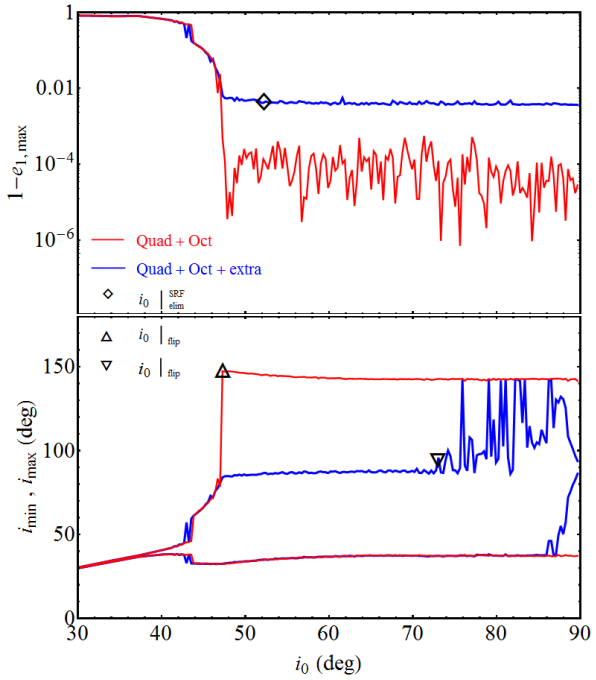

Figure 10. Case 10b in Table 1 ($\varepsilon_{\rm Oct} = 0.067$, $\varepsilon_{\rm GR} = 2.37 \times 10^{-4}$, $\varepsilon_{\rm Tide} = 1.39 \times 10^{-9}$). System parameters are $m_0 = 1M_\odot$, $m_1 = 1M_J$, $m_2 = 1M_\odot$ $a_1 = 1$AU and $a_2 = 33.33$AU. Orbits are started with $e_1 = 0.001$, $e_2 = 0.8$, $\omega_1 = 0°$, $\omega_2 = 0°$, $\Omega_1 = 0°$ and $\Omega_2 = 180°$. The total integration time is 5×10^5 years ($\sim 392.5\ t_K$). Note that $e_{\rm lim}$ decreases, the critical angles ($i_0|^{\rm SRF}_{\rm elim}$ and $i_0|^{\rm SRF}_{\rm flip}$) are pushed to higher values.

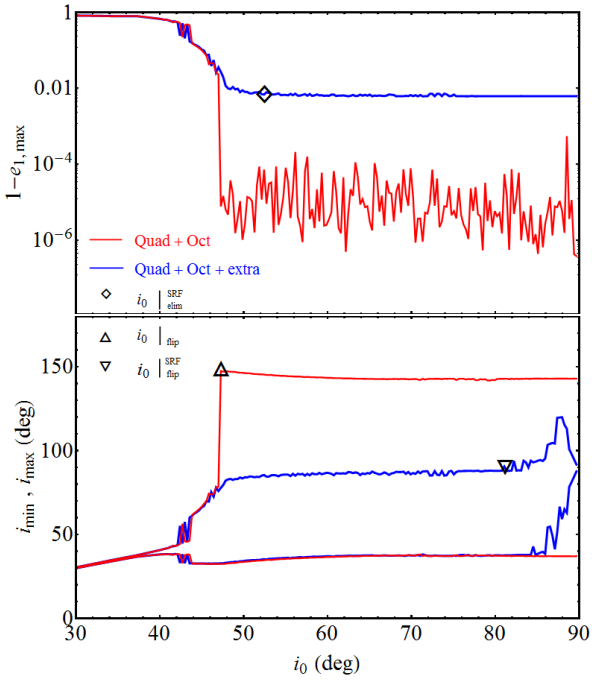

Figure 11. Case 10c in Table 1 ($\varepsilon_{\rm Oct} = 0.067$, $\varepsilon_{\rm GR} = 2.37\times10^{-3}$, $\varepsilon_{\rm Tide} = 1.39 \times 10^{-8}$). System parameters are $m_0 = 1M_\odot$, $m_1 = 1M_J$, $m_2 = 0.1M_\odot$ $a_1 = 1$AU and $a_2 = 33.33$AU. Orbits are started with $e_1 = 0.001$, $e_2 = 0.8$, $\omega_1 = 0°$, $\omega_2 = 0°$, $\Omega_1 = 0°$ and $\Omega_2 = 180°$. The total integration time is 5×10^6 years ($\sim 392.5\ t_K$). The value of $e_{\rm lim}$ becomes smaller than in Case 10b and the maximum inclination angle cannot reach 140°.

different values of the parameters $\varepsilon_{\rm Oct}$, $\varepsilon_{\rm GR}$, $\varepsilon_{\rm Tide}$, $\varepsilon_{\rm Rot}$ (see Table 1). In particular, the dimensionless octupole parameter $\varepsilon_{\rm Oct}$ can be varied by changing the values of e_2 and the ratio of a_1 to a_2 (see Equation 10), and we consider $\varepsilon_{\rm Oct}$ ranging from 0.001 to 0.1. For a given $\varepsilon_{\rm Oct}$, we consider various possible values of $\varepsilon_{\rm GR}$, $\varepsilon_{\rm Tide}$, $\varepsilon_{\rm Rot}$ (see Equations 33, 35 and 39) in order to assess the role of SRFs. For each set of parameters and the initial inclination angle i_0, we integrate the binary evolution equations for a few octupole oscillation periods, $t_K/\varepsilon_{\rm Oct}$, and record the maximum of e_1 and the extrema of $i_{\rm tot}$ attained during the evolution. Table 2 summarizes our key findings.

As noted before (Section 4.1), the SRFs provide an upper limit to the maximum eccentricity attainable during the binary evolution, even for large $\varepsilon_{\rm Oct}$. In particular, our numerical result for the maximum eccentricity $e_{\rm max,Num}$ (for all i_0's) is in good agreement with the limiting eccentricity $e_{\rm lim}$ given by Equation (56). Comparing $\dot\omega_{\rm extra}/\dot\omega_{\rm K}$ at $e_1 = e_{\rm lim}$, we see that with the exception of Case 1, the tidal effect and the rotational bulge are responsible for limiting the eccentricity growth.

The last three columns of Table 2 summarize the three critical initial inclination angles introduced in Section 4.1 for the different cases. Without SRFs, the angle $i_0|_{\rm flip}$ (at which orbital flip occurs due to the octupole potential) decreases with increasing $\varepsilon_{\rm Oct}$. When the SRFs are included, orbital flips require higher inclinations ($i_0|^{\rm SRF}_{\rm flip} > i_0|_{\rm flip}$), and the critical angle $i_0|^{\rm SRF}_{\rm flip}$ decreases as $\varepsilon_{\rm Oct}$ increases. Note that when $\varepsilon_{\rm Oct} \lesssim 0.02$ (Case 1 to Case 6), $i_0|^{\rm SRF}_{\rm flip} \approx 90°$, implying that the octupole potential cannot lead to orbit flip. Finally, in the presence of the SRFs, the critical inclination $i_0|^{\rm SRF}_{\rm elim}$ at which the maximum eccentricity saturates to $e_{\rm lim}$ is roughly equals to $i_0|_{\rm flip}$. This implies that the excitations of eccentricity and inclination are related.

Figures 9–11 depict the results for Case 10a-10c, corresponding to the same $\varepsilon_{\rm Oct}$ but different SRF strength. Note that, as $\varepsilon_{\rm Oct}$ is the same for all these examples, the width of the octupole window of influence is unaltered. However, the region in inclination angle for which orbits are allowed to flip changes with $\varepsilon_{\rm extra}$. This is quantified by the value of the critical angle $i_0|^{\rm SRF}_{\rm flip}$, which grows monotonically with $\varepsilon_{\rm extra}$, meaning that orbital flips are progressively confined to the neighboring region of $i_0 = 90°$.

5 NUMERICAL EXPERIMENTS IN THE COMPARABLE MASS REGIME

In this section, we extend the analysis of previous sections to the general case of Lidov–Kozai cycles with SRFs in systems composed of three comparable masses ($m_0 \sim m_1 \sim m_2 \sim m_\odot$), focusing on the long term evolution of eccentricity and inclination of the inner binary.

5.1 Symmetry in inclination at the quadrupole-level approximation

As discussed in Section 2.3, the equations of motion in the test-particle limit are symmetric upon reflections of the $\mathbf{j}_1$

vector through the origin. This implies that the Lidov–Kozai cycles with SRFs examples in the small mass regime ($m_1 \ll m_0$) presented in Figures 7–11 show even symmetry around $i_0 = 90^\circ$ in the eccentricity curves (top panels) and odd symmetry in the inclination curves (bottom panels). As we have shown in a previous example (Figure 2), this reflection symmetry is removed when $m_1 \sim m_0$.

However, there is still an approximate symmetry center for calculations at the quadrupole-level. This can be seen in Figure 12 for a triple system of comparable masses. In a similar fashion to Figures 7–11, the black curves in Figure 12 show $e_{1,\max}$ and $i_{1,\max/\min}$ as a function of $i_{1,0}$ and $i_{\rm tot,0}$ calculated from the quadrupole-level potential. We have extended the initial inclinations to cover (0°,180°), encompassing the full range of prograde and retrograde orientations. There is a reflection symmetry respect to $i_{\rm tot,0} \approx 94.5^\circ$ (or equivalently, respect to $i_{1,0} \approx 85.5^\circ$). However, this symmetry is erased once octupole-level terms are considered (red curves). This is in contrast to the test-particle limit, for which the reflection symmetry around $i_{\rm tot,0} = i_{1,0} = 90^\circ$ is valid for the quadrupole-level and octupole-level approximations.

The shift in the symmetry center away from 90° results from the conservation of total angular momentum and the quadrupole-level potential. Introducing the total angular momentum $G_{\rm tot}$, we can write the mutual inclination of the inner and outer orbits as (Naoz et al. 2013b)

$$\cos i_{\rm tot} = \frac{G_{\rm tot}^2 - L_1^2(1-e_1^2) - L_2^2(1-e_2^2)}{2L_1L_2\sqrt{1-e_1^2}\sqrt{1-e_2^2}} \ , \qquad (59)$$

where L_1 and L_2 are given by Equations (15)–(16). Since $G_{\rm tot}$ is conserved, this expression becomes

$$\cos i_{\rm tot} = \frac{\cos i_{\rm tot,0}}{\sqrt{1-e_1^2}} + \frac{L_1}{2L_2}\frac{e_1^2}{\sqrt{1-e_1^2}\sqrt{1-e_{2,0}^2}} \ , \qquad (60)$$

where $i_{\rm tot,0}$, $e_{1,0} = 0$ and $e_{2,0}$ are the initial values for the mutual inclination and for the inner and outer eccentricities, respectively. Note that, at the quadrupole level, the eccentricity of the outer orbit $e_2 = e_{2,0} =$ constant. Next, we rewrite the (constant) potential of Equation (49) as

$$\begin{aligned} -\frac{8\langle\Phi_{\rm Quad}\rangle}{\mu_1\Phi_0} &= 3\cos^2 i_{\rm tot}(1+4e_1^2) - 1 - 9e_1^2 \\ &\quad + 15e_1^2\cos^2\omega_1(1-\cos^2 i_{\rm tot}) \ . \end{aligned} \qquad (61)$$

Combining Equations (60) and (61), we obtain an expression for the maximum eccentricity $e_{1,\max}$ (after evaluating at $\omega_1 = \pi/2$):

$$\begin{aligned} &5\cos^2 i_{\rm tot,0} - 3 + \frac{L_1}{L_2}\frac{\cos i_{\rm tot,0}}{\sqrt{1-e_{2,0}^2}} + \left(\frac{L_1}{L_2}\right)^2\frac{e_{1,\max}^4}{1-e_{2,0}^2} \\ &+ e_{1,\max}^2\left[3 + 4\frac{L_1}{L_2}\frac{\cos i_{\rm tot,0}}{\sqrt{1-e_{2,0}^2}} + \left(\frac{L_1}{2L_2}\right)^2\frac{1}{1-e_{2,0}^2}\right] = 0 \ . \end{aligned} \qquad (62)$$

Equation (62) generalizes Equation (51) for the test-mass case. These two expressions become equivalent in the limit $L_1/L_2 \to 0$.

In the test-particle limit at the quadrupole level, the symmetry center (at $i_0 = 90^\circ$) coincides with the point of maximal "eccentricity" or $e_{1,\max} = 1$. Similarly, for the general case of comparable masses, we define the angle $i_{\rm tot,0}|_{\rm sym}$ by setting $e_{1,\max} = 1$ in Equation (62):

$$\cos i_{\rm tot,0}|_{\rm sym} = -\frac{1}{2}\frac{L_1}{L_2}\frac{1}{\sqrt{1-e_{2,0}^2}} \ . \qquad (63)$$

As expected, in the limit $L_1/L_2 \to 0$ we have that $i_{\rm tot,0}|_{\rm sym} \to 90^\circ$. Note that the negative sign in Equation (63) implies that $i_{\rm tot,0}|_{\rm sym}$ is always greater than 90°. This symmetry breaking can also be realized for the inner inclination i_1, which can be obtained from conservation of angular momentum and the law of sines: $L_1(1-e_{1,0}^2)^{1/2}/\sin i_{2,0} = G_{\rm tot}/\sin i_{\rm tot,0} = L_2(1-e_{2,0}^2)^{1/2}/\sin i_{1,0}$. This is consistent with the numerical result shown in Figure 12.

5.2 Parameter space

Figures 12–15 show the dependence of maximum eccentricity and inclination extrema as a function of $i_{1,0}$ (or $i_{\rm tot,0}$) for systems with different masses $m_0 = 1M_\odot$, $m_1 = 0.5M_\odot$ and other parameters. As in the examples of Section 4, four different calculations shown: (1) quadrupole-level approximation with no SRFs (black curves), (2) octupole-level approximation with no SRFs (red curves), (3) quadrupole-level approximation with SRFs (green curves), and (4) octupole-level approximation with SRFs (blue curves).

Just as in Section 4, we explore the changes in $e_{1,\max}$ and $i_{1,\max/\min}$ as we vary $\varepsilon_{\rm Oct}$ and $\varepsilon_{\rm extra}$, this time for triple stars of comparable masses. Note that in Equation (10), the octupole contribution is exactly zero if the members of inner binary here equal mass, so for similar masses, $\varepsilon_{\rm Oct}$ cannot be very large. The orbital separations and other physical parameters of the systems studied in this section are listed in Table 3.

The values of initial inclinations induced both prograde and retrograde orbits in $i_{1,0}$ (i.e., respect to the total angular momentum vector). The range in angles is chosen so as to enclose the "Lidov–Kozai active" region. This region is contained between the angles $i_{\rm tot,0}|_{\rm st}^-$ and $i_{\rm tot,0}|_{\rm st}^+$, which are the two solutions of the quadratic equation obtained from Equation (62) after setting $e_{1,\max} = 0$:

$$5\cos^2 i_{\rm tot,0}|_{\rm st} - 3 + \frac{L_1}{L_2}\frac{\cos i_{\rm tot,0}|_{\rm st}}{\sqrt{1-e_{2,0}^2}} = 0 \ . \qquad (64)$$

For all the examples considered here (Table 3), an inclination interval of $i_{1,0} \in (30^\circ, 150^\circ)$ is sufficient to capture the entire range of systems that are subject to Lidov–Kozai oscillations.

5.2.1 Eccentricity maxima

As discussed in Section 5.1 above, for finite m_1, the symmetry of the system respect to $i_{\rm tot,0} = 90^\circ$ is shifted to a different value $i_{\rm tot,0}|_{\rm sym}$. However, this symmetry center only reflects the behaviour of the system at the quadrupole level. In addition to the significant when the octupole potential is included, Figure 12 (for $\varepsilon_{\rm Oct} = 0.022$) also shows how the symmetry between prograde and retrograde orbits is broken.

Table 3. Initial conditions on different cases: $m_0 = 1M_\odot$, $e_0 = 0.001$, $k_{2,1} = 0.014$, $\omega_1 = \omega_2 = \Omega_1 = 0^\circ$ and $\Omega_2 = 180^\circ$. The parameter $\varepsilon_{\rm extra}$ is calculated from the definition in Equations (33) and (35).

Parameter	$\varepsilon_{\rm Oct}$	$\varepsilon_{\rm GR}$	$\varepsilon_{\rm Tide}$	a_1(AU)	a_2(AU)	$e_{2,0}$	$m_1(M_\odot)$	$m_2(M_\odot)$	$R_1(R_\odot)$
Case 1a	0.022	4.33×10^{-6}	4.00×10^{-16}	10	100	0.5	0.5	1	0.5
Case 1b	0.022	1.44×10^{-5}	1.64×10^{-13}	3	30	0.5	0.5	1	0.5
Case 1c	0.022	4.33×10^{-5}	4.00×10^{-11}	1	10	0.5	0.5	1	0.5
Case 1d	0.022	4.33×10^{-5}	4.10×10^{-8}	1	10	0.5	0.5	1	2
Case 1e	0.022	4.33×10^{-5}	4.00×10^{-6}	1	10	0.5	0.5	1	5
Case 2a	0.042	5.53×10^{-6}	7.64×10^{-17}	10	120	0.6	0.3	0.8	0.3
Case 2b	0.042	1.11×10^{-5}	2.45×10^{-15}	5	60	0.6	0.3	0.8	0.3
Case 2c	0.042	5.53×10^{-5}	7.64×10^{-12}	1	12	0.6	0.3	0.8	0.3
Case 2d	0.042	5.53×10^{-5}	2.45×10^{-10}	1	12	0.6	0.3	0.8	0.6
Case 2e	0.042	5.53×10^{-5}	9.83×10^{-6}	1	12	0.6	0.3	0.8	5

Table 4. Results on different cases. $i_{1,0}|_{\rm sym}$ is the initial inclination where $e_{1,\rm max}$ reaches the maximum at the quadrupole level. While $i_{\rm tot,0}|_{\rm sym}$ is for total initial angle.

Parameter	$1-e_{\rm lim}$	$1-e_{\rm max,Num}$	$\frac{\dot\omega_{\rm GR}}{\dot\omega_{\rm K}}\big\vert_{e_{\rm lim}}$	$\frac{\dot\omega_{\rm Tide}}{\dot\omega_{\rm K}}\big\vert_{e_{\rm lim}}$	$i_{1,0}\vert_{\rm sym}$(deg)	$i_{\rm tot,0}\vert_{\rm sym}$(deg)
Case 1a	1.40×10^{-4}	1.39×10^{-4}	2.58×10^{-4}	10.12	85.5	94.5
Case 1b	5.35×10^{-4}	5.27×10^{-4}	4.43×10^{-4}	10.11	85.5	94.5
Case 1c	1.81×10^{-3}	1.80×10^{-3}	7.19×10^{-4}	10.09	85.5	94.5
Case 1d	8.50×10^{-3}	8.46×10^{-3}	3.33×10^{-4}	9.98	85.5	94.5
Case 1e	2.37×10^{-2}	2.36×10^{-2}	2.00×10^{-4}	9.74	85.5	94.5
Case 2a	9.71×10^{-5}	9.57×10^{-5}	3.97×10^{-4}	10.12	86.2	93.8
Case 2b	2.10×10^{-4}	2.06×10^{-4}	5.40×10^{-4}	10.12	86.2	93.8
Case 2c	1.26×10^{-3}	1.22×10^{-3}	1.10×10^{-3}	10.10	86.2	93.8
Case 2d	2.71×10^{-3}	2.64×10^{-3}	7.52×10^{-4}	10.07	86.2	93.8
Case 2e	2.90×10^{-2}	2.89×10^{-2}	2.31×10^{-4}	9.65	86.2	93.8

Figure 12 shows that at the quadrupole level, the excitation of eccentricity only takes place in the range between $i_{\rm tot,0}|_{\rm st} = 40.4^\circ$ and $i_{\rm tot,0}|_{\rm st} = 142.0^\circ$, as given by Equation (64), and $e_{1,\rm max}$ is achieved at $i_{\rm tot,0}|_{\rm sym} \approx 85.5^\circ$ (Table 4), as predicted by Equation (63). When the octupole-level terms are included (red curve), $i_{\rm tot,0} \approx 85.5^\circ$ is not the only inclination that allows for such extreme eccentricity (i.e., $e_{1,\rm max} \approx 1$). Indeed, as in the test-mass case (Figures 7–11), the inclusion of octupole terms widens the range on angles for which $e_1 \to 1$ is possible. In this case however, the "widening" takes place to the right of $i_{\rm tot,0}|_{\rm sym}$, while the quadrupole-level solution remains valid for $i_{1,0} < i_{\rm tot,0}|_{\rm sym}$ down to for $i_{1,0} \sim 75^\circ$. Below $\sim 75^\circ$, deviations from the quadrupole-level solution become significant. These features, which can be compared to what seemed to be minor fluctuations in $e_{1,\rm max}$ for the test-particle cases (see Figures 7–11), show that moderately high eccentricities can be excited at lower inclinations ($i_{\rm tot,0} = 60^\circ \sim 80^\circ$) than the quadrupole-order calculation would allow.

When SRFs are included, the quadrupole-level eccentricity maxima are truncated at a global maximum corresponding to $1-e_{1,\rm max} \sim 10^{-3}$. The horizontal line in Figure 12 corresponds to the limiting eccentricity given by Equation (56). It is important to note that this limiting eccentricity applies even in the general case of comparable masses. Also note that the tides are mainly responsible for the eccentricity suppression (see Table 4).

It is not surprising that the analytic estimate of $e_{\rm lim}$, derived in the test-mass limit (Section 3.3), remains a good approximation for comparable-mass systems. For e_1 very close to unity, the vast majority of the angular momentum resides in the outer binary, forcing the inner binary to behave essentially as a test particle. Note that we can use Equations (17), (19) and (20) at the quadrupole level ($\varepsilon_{\rm Oct} = 0$) to write

$$\frac{d}{dt}\big(\mathbf{j}_1\cdot\hat{\mathbf{n}}_2\big) = \frac{1}{\sqrt{1-e_2^2}}\,\mathbf{j}_1\cdot\frac{d\mathbf{j}_2}{dt} = \frac{15}{4t_K}\frac{L_1\sqrt{1-e_1^2}}{L_2\sqrt{1-e_2^2}}e_1^2(\hat{\mathbf{u}}_1\cdot\hat{\mathbf{n}}_2)(\,\hat{\mathbf{u}}_1\times\hat{\mathbf{n}}_2)\cdot\hat{\mathbf{n}}_1\ , \tag{65}$$

where all the vectors involved are of norm unity. Then we find that $d\big(\mathbf{j}_1\cdot\hat{\mathbf{n}}_2\big)/dt$ is very small provided that $L_2\sqrt{1-e_2^2} \gg L_1\sqrt{1-e_1^2}$. Therefore, for the high eccentricity phase of Lidov–Kozai cycles, the analysis of Section 3.3 for test particles still applies in the comparable-mass regime. As in the test-mass cases (Section 4), the octupole effect expands the range of the initial mutual inclinations capable of reaching maximal eccentricities.

5.2.2 Inclination extrema

As for the eccentricity curves, the inclination curves at the quadrupole level in Figure 12 (black curves) are symmetric respect to $i_{1,0}|_{\rm sym}$. In this particular example, SRFs do not

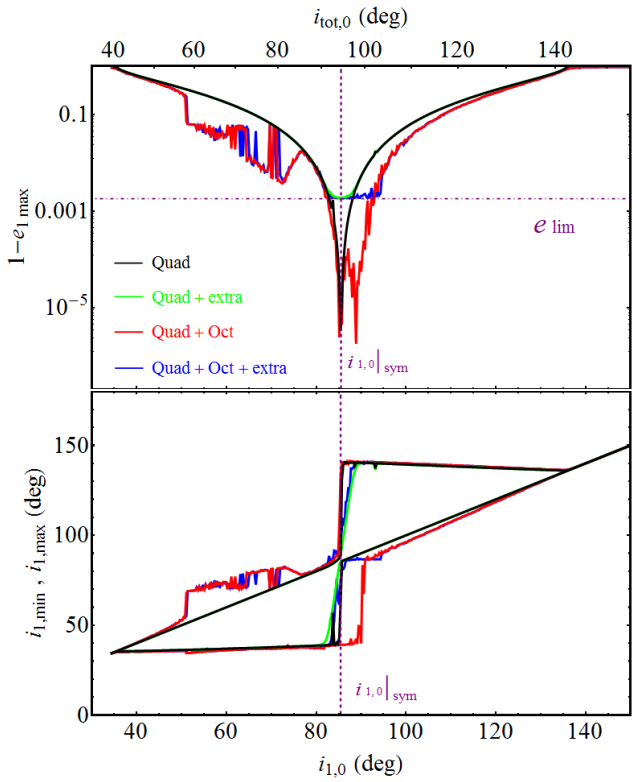

Figure 12. CASE 1c of Table 3. $\varepsilon_{\rm Oct} = 0.022$. We extend the test-particle case in Section 4 to comparable-mass case. Here, the system has an inner binary of $m_0 = 1M_\odot$, $m_1 = 0.5M_\odot$, $a_1 = 1$AU, $R_1 = 0.5R_\odot$ and the companion has $m_2 = 1M_\odot$, $a_2 = 10$AU. We initially set $e_1 = 0.001$, $e_2 = 0.5$, $\omega_1 = 0°$, $\omega_2 = 0°$, $\Omega_1 = 0°$ and $\Omega_2 = 180°$. Because there is no reflection symmetry between the prograde and retrograde configurations, we integrate Equations (A1)-(A7) with $i_{1,0} \in (30°, 150°)$ for 5×10^4 years ($\sim 395.0 t_K$). Note that limiting eccentricity holds as well and the flip cannot occur with SRFs.

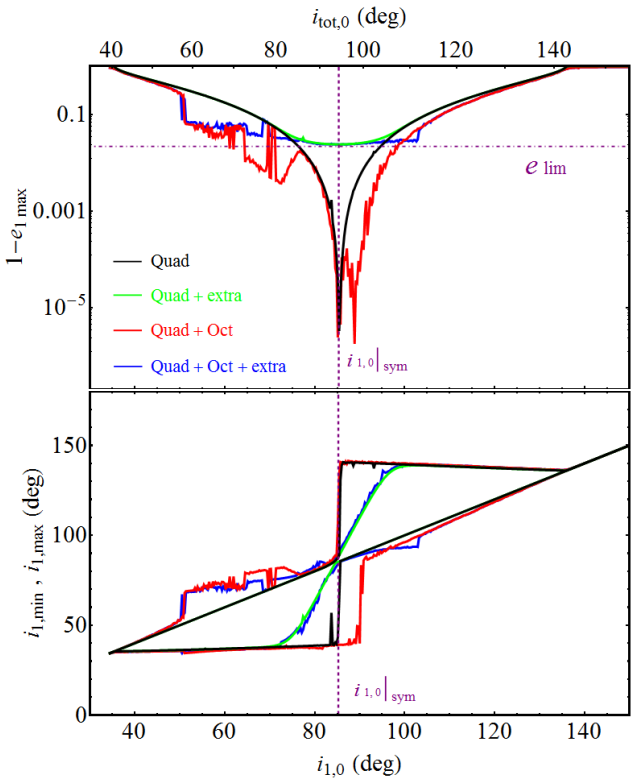

Figure 13. CASE 1e of Table 3. We increase $\varepsilon_{\rm extra}$ by changing $a_1 = 1$AU, $a_2 = 10$AU and $R_1 = 5R_\odot$, and keep other quantities the same as Case 1c (See Table 3). We integrate the equations and the total integration time is 5×10^4 years ($\sim 395.0 t_K$). Note that $e_{\rm lim}$ become smaller and SRFs affect the octupole-level effects significantly.

inflict significant modifications except for the close vicinity of $i_{1,0}|_{\rm sym}$, which sees the amplitude in the inclination oscillations (the difference between $i_{1,\rm min}$ and $i_{1,\rm max}$) reduced (green curves).

At the octupole level (red curves), the asymmetries that arise in the eccentricity curve find their counterpart in the inclination curves. Within a narrow range of angles (rightward of $i_{1,0}|_{\rm sym}$), the orbits are allowed to flip from retrograde to prograde. For initial inclinations bellow $i_{1,0} \sim 70°$, although the octupole potential introduces significant changes in $1 - e_{1,\rm max}$ and $i_{1,\rm max/min}$, it is not strong enough to cause orbital flips. In accordance to what is observed in the eccentricity curves, the octupole contributions to the left of $i_{1,0}|_{\rm sym}$ are not affected by SRF, however, the flips observed for angles $i_{1,0} > i_{1,0}|_{\rm sym}$ is nearly entirely suppressed by the inclusion of these additional effects (blue curves).

5.2.3 Dependence on $\varepsilon_{\rm Oct}$ and $\varepsilon_{\rm extra}$

The example of Figure 12 shows moderate differences in maximum eccentricity and inclination range between the quadrupole and the octupole-level solutions. To explore the behaviour of these variables for larger octupole contributions we integrate systems with $\varepsilon_{\rm Oct} = 0.042$ varying the magnitude of $\varepsilon_{\rm extra}$ (Table 3). Some of these examples are shown in Figure 14 and 15.

The most important difference between the top panels of Figure 14 and Figure 12 is the width of the maximal eccentricity region to the right of $i_{1,0}|_{\rm sym}$ (this was already observed in the examples of Section 4) and the deepening of the high eccentricity region to the left of $i_{1,0}|_{\rm sym}$. As $\varepsilon_{\rm Oct}$ is increased, the asymmetries between the prograde and retrograde regions of the figure become more pronounced. Prograde orbits at intermediate inclination see their maximum eccentricities increase, to a point that they become comparable to those seen for the retrograde orbits. It is at this point (when $1 - e_{1,\rm max} \lesssim 10^{-4}$) that prograde orbits are allowed to flip orientations.

When SRFs are considered, the maximum eccentricities (green and blue curves) are altered in a similar fashion as the example of Figure 12. The value of $e_{\rm lim}$ of Equation (56) is still in agreement with the global maximum of $e_{1,\rm max}$ (See Table 4). On the other hand, the growth of $i_{1,\rm max}$ is suppressed (no flip) in prograde configurations, while $i_{1,\rm min}$ appears to vary erratically when $i_{1,0} > i_{1,0}|_{\rm sym}$ (See Figure 14).

Figures 13 and 15 show examples of increased $\varepsilon_{\rm extra}$ for the same $\varepsilon_{\rm Oct}$ as in Figures 12 and 14. In these cases, $e_{\rm lim}$ is smaller than in Case 2c (Figure 14), which implies that SRFs are truncating $e_{1,\rm max}$ not only in the vicinity of $i_{\rm tot,0}|_{\rm sym}$, but

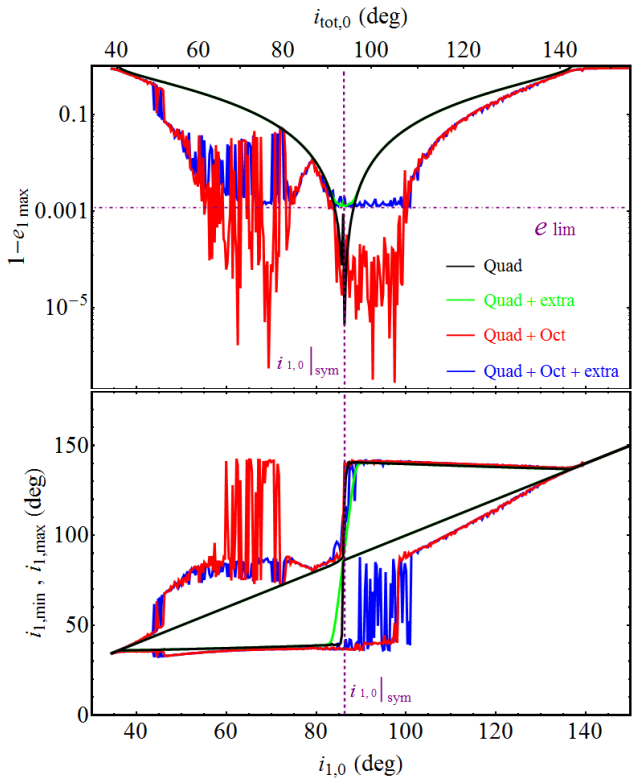

Figure 14. CASE 2c of Table 3. We carry out another set of numerical integrations with higher $\varepsilon_{\rm Oct} = 0.042$. The system has an inner binary of $m_0 = 1M_\odot$, $m_1 = 0.3M_\odot$, $a_1 = 1$AU, $R_1 = 0.3R_\odot$ and the companion has $m_2 = 0.8M_\odot$, $a_2 = 12$AU. We initially set $e_1 = 0.001$, $e_2 = 0.6$,$\omega_1 = 0°$, $\omega_2 = 0°$, $\Omega_1 = 0°$ and $\Omega_2 = 180°$. We integrate the equations for 1.2×10^5 years ($\sim 598.0 t_K$). Due to the stronger octupole potential, the width of the $e_{1,\rm max}$ and $i_{0,\rm max/min}$ regions become lager and the flip occur even with SRFs.

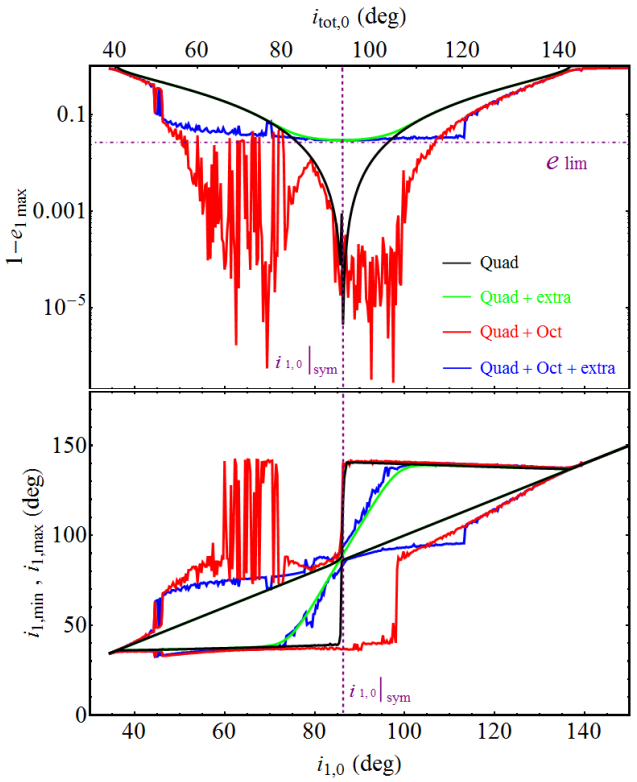

Figure 15. CASE 2e of Table 3. Results of numerical integrations with higher $\varepsilon_{\rm extra}$. The system has an inner binary of $m_0 = 1M_\odot$, $m_1 = 0.3M_\odot$, $a_1 = 1$AU, $R_1 = 5R_\odot$ and the companion has $m_2 = 0.8M_\odot$, $a_2 = 12$AU. We initially set $e_1 = 0.001$, $e_2 = 0.6$, $\omega_1 = 0°$, $\omega_2 = 0°$, $\Omega_1 = 0°$ and $\Omega_2 = 180°$. The total integration time is 1.2×10^5 years ($\sim 598.0 t_K$).

also in the lower inclination region [$i_{1,0} \in (55°, 75°)$], thus affecting the octupole-level effects significantly. Despite the significant restrictions on $e_{1,\rm max}$ imposed by SRFs, the octupole effects cannot be neglected for their values of $\varepsilon_{\rm Oct}$, since they allow for these systems to reach eccentricities with $1 - e_{\rm lim} \sim 5 \times 10^{-2}$ for initial mutual inclinations as low as $i_{\rm tot,0} \sim 55°$ (Figure 15) while the quadrupole-level calculation would require inclinations beyond 75° to reach similar values.

6 SUMMARY AND CONCLUSIONS

In this paper, we have computed the extent to which energy-conserving short-range effects alter the orbital evolution of planets and stars in hierarchical triple systems undergoing Lidov-Kozai oscillations. In particular, we have systematically examined how general relativistic precession, tides and oblateness can moderate the extreme values in eccentricity and inclination that can be achieved owing to the octupole terms in the interaction potential.

By carrying of a sequence of numerical experiments, we have measured the extrema in eccentricity and inclination for a variety of hierarchical triples, systematically varying the relative strengths of the octupole terms and of the short-range effects in terms of their contributions to the potential energy. The results of our calculations can be summarized into four main findings.

(1) The importance of the octupole effects depends on the dimensionless parameter $\varepsilon_{\rm Oct}$ (see Equation 10), which measures the relative strength between the octupole and quadrupole potentials. The main contribution of the octupole terms to eccentricity and inclination excitation is limited to a range in initial inclinations or "window of influence", the width of which grows with $\varepsilon_{\rm Oct}$. As $\varepsilon_{\rm Oct}$ decreases, the window of influence becomes increasingly confined to mutual inclinations close to 90°. For example, at $\varepsilon_{\rm Oct} \sim 0.002$, the octupole terms are important only within a few degrees around $i_{tot,0} = 90°$ (see Tables 1 and 2; also see Fig. 8).

(2) We find that short range forces can indeed compete with the octupole-level terms in the potential, and that these additional effects impose a strict upper limit on the maximum achievable eccentricity. Most importantly, we find that to a very good approximation, this maximum eccentricity can be derived analytically using the quadrupole approximation in the test-particle limit (see section 3.3 and Equation 56). This analytic limiting eccentricity holds even for a strong octupole contribution as well as in the general case of three comparable masses.

(3) Our results indicate that, despite the upper limit in eccentricity (which is independent on the octupole strength),

the width of the window of influence of the octupole potential (see point 1 above) is largely unaffected by the SRFs.

(4) We find that orbital flips are affected by the SRFs. With increasing strength of the SRFs (characterized by the dimensionless parameters; see Equations 33, 35 and 39), orbital flips are increasingly confined to the region close to $i_{\rm tot,0} = 90^\circ$ (see Figs. 9–11 and Tables 1-2).

ACKNOWLEDGMENTS

This work has been supported in part by NSF grant AST-1211061, and NASA grants NNX12AF85G, NNX14AG94G and NNX14AP31G. DJM thanks Boaz Katz and Cristóbal Petrovich for helpful discussions. BL gratefully acknowledges support from the China Scholarship Council.

REFERENCES

Alexander M. E., 1973, ASS, 23, 459
Antonini F., Murray N., Mikkola S., 2014, ApJ, 781, 45
Blaes O., Lee M. H., Socrates A., 2002, ApJ, 578, 775
Carruba V., Burns J. A., Nicholson P. D., Gladman B. J., 2002, Icar, 158, 434
Correia A. C. M., Laskar J., Farago F., Boue G., 2011, Celest. Mech. Dynamical Astron., 111, 105
Dong S., Katz B., Socrates A., 2014, ApJ, 781, LL5
Eggleton P. P. & Kiseleva–Eggleton L., 2001, ApJ, 562, 1012
Fabrycky D. C., Tremaine S. 2007 ApJ 669 1298
Ford E. B., Kozinsky B., Rasio F. A., 2000b, ApJ, 535, 385
Harrington R. S., 1968, AJ, 73, 190
Holman M., Touma J., Tremain S., 1997, Nat, 386, 254
Hut P., 1981, A&A, 99, 126
Innanen K. A., Zheng J. Q., Mikkola S., Valtonen M. J., 1997, AJ, 113, 1915
Katz B., Dong S., Malhotra R., 2011, PhRvL, 107, 181101
Katz B., Dong S., 2012, preprint(arXiv:1211.4584)
Kiseleva L. G., Eggleton P. P., Mikkola S., 1998, MNRAS, 300, 292
Kozai Y., 1962, AJ, 67, 591
Krymolowski Y., Mazeh T., 1999, MNRAS, 304, 720
Kushnir D., Katz B., Dong S., Livne E., Fernández R., 2013, ApJ, 778, L37
Li G., Naoz S., Kocsis B., Loeb A., 2014, ApJ, 785, 116
Li G., Naoz S., Holman M., Loeb A., 2014, ApJ, 791, 86
Lidov M. L., 1962, Planet. Space Sci., 9, 719
Lithwick Y., Naoz S., 2011, ApJ, 742, 94
Marchal C., 1990, The Three-Body Problem. Elsevier Sci., Amsterdam
Mardling R. A., Aarseth S.J., 2001, MNRAS, 321, 398
Mazeh T., Krymolowski Y., Rosenfeld G., 1997, ApJ 477, L103
Mazeh T., Shaham J., 1979, A&A 77, 145
Miller M. C., Hamilton D.P., 2002, ApJ, 576, 894
Murray C. D., Dermott S. F., 1999, Cambridge University Press
Naoz S., Farr W. M., Lithwick Y., Rasio F. A., Teyssandier J., 2011, Nat, 473, 187
Naoz S., Farr W. M., Rasio F. A., 2012, ApJ, 754, L36
Naoz S., Farr W. M., Lithwick Y., Rasio F. A., 2013b, MNRAS, 431, 2155
Naoz S., Fabrycky D. C. 2014, preprint(arXiv:1405.5223)
Nesvorný D., Alvarellos J. L. A., Dones L., Levison H. F., 2003, AJ, 126, 398
Perets H. B., Fabrycky D. C., 2009, ApJ, 697, 1048
Petrovich C., 2014, preprint(arXiv:1405.0280)
Prodan S., Murray N., Thompson T. A., 2013, preprint(arXiv:1305.2191)
Shappee B. J., Thompson T. A., 2013, ApJ, 766, 64
Storch, N. I., Anderson, K. R., & Lai, D. 2014, *Science*, 345, 1317, preprint(arXiv:1409.3247)
Teyssandier J., Naoz S., Lizarraga I., Rasio F. A., 2013, ApJ, 779, 166
Thompson T. A., 2011, ApJ, 741, 82
Tremaine S., Toura J., Namouni F., 2009, AJ, 137, 3706
Tremaine, S., & Yavetz, T. D. 2014, American Journal of Physics, 82, 769
Wen L., 2003, ApJ, 598, 419
Wu Y., Murray N., 2003, ApJ, 589, 605

APPENDIX A: FULL DYNAMIC EQUATIONS

We present the complete secular equations for octupole order in this section obtained from applying the matrix projection (Equations 22 and 23) to the vector-form equations of motion (Equations 17–20). Omitting the laborious matrix manipulation, we get:

$$\begin{aligned}\frac{de_1}{dt} = \frac{\sqrt{1-e_1^2}}{64\ t_K}\Bigg\{ & 120 e_1 \sin^2 i_{\rm tot} \sin 2\omega_1 \\ & + \frac{15\varepsilon_{\rm Oct}}{8}\cos\omega_2\Big[(4+3e_1^2)(3+5\cos 2i_{\rm tot})\sin\omega_1 \\ & + 210 e_1^2 \sin^2 i_{\rm tot}\sin 3\omega_1\Big] \\ & - \frac{15\varepsilon_{\rm Oct}}{4}\cos i_{\rm tot}\cos\omega_1\Big[15(2+5e_1^2)\cos 2i_{\rm tot} \\ & + 7(30e_1^2\cos 2\omega_1 \sin^2 i_{\rm tot} - 2 - 9e_1^2)\Big]\sin\omega_2\Bigg\}\,,\end{aligned} \tag{A1}$$

and

$$\begin{aligned}\frac{de_2}{dt} = \frac{15 e_1 L_1\sqrt{1-e_2^2}\ \varepsilon_{\rm Oct}}{256\ t_K\ e_2\ L_2}\Bigg\{ & \cos\omega_1\Big[6 - 13e_1^2 \\ & + 5(2+5e_1^2)\cos 2i_{\rm tot} + 70 e_1^2\cos 2\omega_1\sin^2 i_{\rm tot}\Big] \\ & \times \sin\omega_2 - \cos i_{\rm tot}\cos\omega_2\Big[5(6+e_1^2)\cos 2i_{\rm tot} \\ & + 7(10e_1^2\cos 2\omega_1\sin^2 i_{\rm tot} - 2 + e_1^2)\Big]\sin\omega_1\Bigg\}\,.\end{aligned} \tag{A2}$$

for the inner and outer eccentricities.

The time evolution of the inclinations are described by

$$\frac{di_1}{dt} = \frac{-3e_1}{32\ t_K\ \sqrt{1-e_1^2}}\Bigg\{10\sin 2i_{\rm tot}\Big[e_1\sin 2\omega_1 + \frac{5\varepsilon_{\rm Oct}}{8}(2+5e_1^2+7e_1^2\cos 2\omega_1)\cos\omega_2\sin\omega_1\Big] + \frac{5\varepsilon_{\rm Oct}}{8}\cos\omega_1\Big[26+37e_1^2-35e_1^2\cos 2\omega_1 - 15\cos 2i_{\rm tot}(7e_1^2\cos 2\omega_1-2-5e_1^2)\Big]\sin i_{\rm tot}\sin\omega_2\Bigg\}\ , \tag{A3}$$

and

$$\frac{di_2}{dt} = \frac{-3e_1L_1}{32\ t_K\ \sqrt{1-e_2^2}\ L_2}\Bigg\{10\Big[2e_1\sin i_{\rm tot}\sin 2\omega_1 + \frac{5\varepsilon_{\rm Oct}}{8}\cos\omega_1(2+5e_1^2-7e_1^2\cos 2\omega_1)\sin 2i_{\rm tot}\sin\omega_2\Big] + \frac{5\varepsilon_{\rm Oct}}{8}\Big[26+107e_1^2+5(6+e_1^2)\cos 2i_{\rm tot} - 35e_1^2(\cos 2i_{\rm tot}-5)\cos 2\omega_1\Big]\cos\omega_2\sin i_{\rm tot}\sin\omega_1\Bigg\}\ . \tag{A4}$$

We also write the longitudes of ascending nodes as a function of time

$$\frac{d\Omega_1}{dt} = \frac{d\Omega_2}{dt} = \frac{-3\csc i_1}{32\ t_K\ \sqrt{1-e_1^2}}\Bigg\{2\Big[(2+3e_1^2-5e_1^2\cos 2\omega_1) + \frac{25\varepsilon_{\rm Oct}e_1}{8}\cos\omega_1(2+5e_1^2-7e_1^2\cos 2\omega_1)\cos\omega_2\Big]\times\sin 2i_{\rm tot} - \frac{5\varepsilon_{\rm Oct}e_1}{8}\Big[35e_1^2(1+3\cos 2i_{\rm tot})\cos 2\omega_1 - 46-17e_1^2-15(6+e_1^2)\cos 2i_{\rm tot}\Big]\sin i_{\rm tot}\sin\omega_1\sin\omega_2\Bigg\}\ . \tag{A5}$$

Finally, the argument of periapse for the inner and outer binaries evolve according to

$$\frac{d\omega_1}{dt} = \frac{3}{8\ t_K}\Bigg\{\frac{1}{\sqrt{1-e_1^2}}\Big[4\cos^2 i_{\rm tot}+(5\cos 2\omega_1-1) \times(1-e_1^2-\cos^2 i_{\rm tot})\Big] + \frac{L_1\cos i_{\rm tot}}{L_2\sqrt{1-e_2^2}}\Big[2+e_1^2(3 - 5\cos 2\omega_1)\Big]\Bigg\} + \frac{15\varepsilon_{\rm Oct}}{64\ t_K}\Bigg\{\left(\frac{L_1}{L_2\sqrt{1-e_2^2}}+\frac{\cos i_{\rm tot}}{\sqrt{1-e_1^2}}\right)\times e_1\Big[\sin\omega_1\sin\omega_2\Big[10(3\cos^2 i_{\rm tot}-1)(1-e_1^2)+A\Big] - 5B\cos i_{\rm tot}\cos\Theta\Big] - \frac{\sqrt{1-e_1^2}}{e_1}\Big[10\sin\omega_1\sin\omega_2\cos i_{\rm tot} \times\sin^2 i_{\rm tot}(1-3e_1^2)+\cos\Theta(3A-10\cos^2 i_{\rm tot}+2)\Big]\Bigg\}\ , \tag{A6}$$

and

$$\frac{d\omega_2}{dt} = \frac{3}{16\ t_K}\Bigg\{\frac{2\cos i_{\rm tot}}{\sqrt{1-e_1^2}}\Big[2+e_1^2(3-5\cos 2\omega_1)\Big] + \frac{L_1}{L_2\sqrt{1-e_2^2}}\Big[4+6e_1^2+(5\cos^2 i_{\rm tot}-3) \times\Big[2+e_1^2(3-5\cos 2\omega_1)\Big]\Big]\Bigg\} - \frac{15\varepsilon_{\rm Oct}e_1}{64\ t_K\ e_2} \times\Bigg\{\sin\omega_1\sin\omega_2\Big[\frac{L_1(4e_2^2+1)}{e_2\ L_2\sqrt{1-e_2^2}}10\cos i_{\rm tot}\sin^2 i_{\rm tot} \times(1-e_1^2)-e_2\left(\frac{1}{\sqrt{1-e_1^2}}+\frac{L_1\cos i_{\rm tot}}{L_2\sqrt{1-e_2^2}}\right) \times\Big[A+10(3\cos^2 i_{\rm tot}-1)(1-e_1^2)\Big]\Big]+\cos\Theta \times\Big[5B\cos i_{\rm tot}e_2\left(\frac{1}{\sqrt{1-e_1^2}}+\frac{L_1\cos i_{\rm tot}}{L_2\sqrt{1-e_2^2}}\right) + \frac{L_1(4e_2^2+1)}{e_2\ L_2\sqrt{1-e_2^2}}A\Big]\Bigg\}\ , \tag{A7}$$

where we define

$$A\equiv 4+3e_1^2-\frac{5}{2}B\sin^2 i_{\rm tot}\ ,\quad B\equiv 2+5e_1^2-7e_1^2\cos 2\omega_1\ , \tag{A8}$$

and

$$\cos\Theta\equiv-\cos\omega_1\cos\omega_2-\cos i_{\rm tot}\sin\omega_1\sin\omega_2\ . \tag{A9}$$